We are IntechOpen, the world's leading publisher of Open Access books
Built by scientists, for scientists

6,900
Open access books available

185,000
International authors and editors

200M
Downloads

Our authors are among the

154
Countries delivered to

TOP 1%
most cited scientists

12.2%
Contributors from top 500 universities

WEB OF SCIENCE™

Selection of our books indexed in the Book Citation Index in Web of Science™ Core Collection (BKCI)

Interested in publishing with us?
Contact book.department@intechopen.com

Numbers displayed above are based on latest data collected.
For more information visit www.intechopen.com

12

Physics of Triangular Graphene

Motohiko Ezawa
Department of Applied Physics, The University of Tokyo
Japan

1. Introduction

Carbon forms many allotropic forms with different dimensionality: three-dimensional diamond, quasi-two-dimensional graphite(1; 2), one-dimensional nanotubes(3–10) and zero-dimensional fullerenes(11). These materials are well known to exhibit remarkable electronic properties depending on their geometry. There exists another form of carbon material, graphene, which is a monolayer graphite. Graphene can theoretically be considered the basic material for the other forms of carbon that can be obtained from it either by stacking (graphite), wrapping (nanotubes), or creation of topological defects (fullerenes). Furthermore, there are many derivatives in these graphene related materials. Their electrical properties, such as carrier type (particle or hole), can be continuously controlled by the application of external gate voltage(12).

Graphite is made out of stacks of graphene layers that are weakly coupled by van der Waals forces. A pencil is a typical graphite. When we use it, we are actually producing graphene stacks on a sheet of paper, which may well contain individual graphene layers. Nevertheless, it was only in 2004 when graphene was experimentally isolated(12). They produced high quality, large (up to 100 μm in size) graphene crystallites, which immediately triggered enormous theoretical and experimental studies. Moreover, the quality of the samples produced are so good that ballistic transport(12) and quantum Hall effects (QHE) have been observed(13; 14). For a recent review on graphene, see ref. (15).

Edge states of graphene show a very remarkable feature. There are three type of edges; zigzag edge, armchair edge and Klein edge(16). Graphene with a zigzag edge has the half-filled flat band at the zero-energy level and exhibits edge ferromagnetism(17). These edge states can be observed by STM(18; 19).

Among graphene derivatives, graphene nanoribbons(17; 20; 21) constitute a fascinating object due to a rich variety of band gaps, from metals to wide-gap semiconductors. In particular, the half-filled zero-energy states emerge in all zigzag nanoribbons and hence they are metallic. Such a peculiar band structure, as recognized by the pioneering work(17) in 1996 and revisited(21) in 2006, has motivated many researchers to investigate their electronic and magnetic properties. Now there are a profusion of papers on them, among which we cite some of early works(22–31). Important works on nanoribbons have been summarized into a map(32) as Essential Science Indicators by Tomson-Reuter in late 2008. Nanoribbons can be manufactured by patterning based on nanoelectronic lithography methods(26; 27; 33).

Another basic element of graphene derivatives is a graphene nanodisk(35; 36). It is a nanometer-scale disk-like material which has a closed edge. It is also referred to as nanoisland(37), nanoflake(38–40), nanofragment(41) or graphene quantum dot(42; 43).

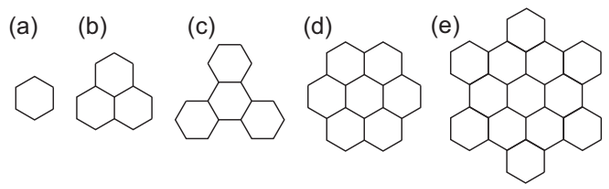

Fig. 1. Basic configurations of typical graphene nanodisks. (a) Benzene. (b) Trigonal zigzag nanodisk (phenalene). (c) Trigonal armchair nanodisk (triphenylene). (d) Hexagonal zigzag nanodisk (coronene). (e) Hexagonal armchair nanodisk (hexa benzocoronene)(34).

Nanoribbons and nanodisks correspond to quantum wires and quantum dots, respectively. They are candidates of future carbon-based nanoelectronics and spintronics alternative to silicon devices. A merit is that a nanoribbon-nanodisk complex can in principle be fabricated, embodying various functions, only by etching a graphene sheet.

There are many types of nanodisks, as displayed in Fig.1. It is possible to manufacture them by etching a graphene sheet by Ni nanoparticles(44). Among them, trigonal zigzag nanodisks are prominent in their electronic property because there exist half-filled zero-energy states in the non-interacting regime(36). This novel electric property was revealed first by the tight-binding model(36) in 2007, and then by first-principle calculations by other groups(37; 38; 45). Various remarkable properties of nanodisks have been investigated extensively in a series of works(36; 46–48).

Although there are yet only a few works on nanodisks, an experimental realization(44) must accelerate both experimental and theoritical studies on them. In this sense, the study of graphene nanodisk is very timely.

It has long been known(49–51) that the physics of electrons near the Fermi energy is described by the massless two-component Dirac equation or the Weyl equation in graphene. Graphene nanoribbons were successfully analyzed based on the Weyl equation in 2006(22). It is straightforward to generalize the method to investigate the structure of the zero-energy states in graphene nanodisks(48). Wave functions are explicitly constructed, which exhibits a texture of magnetic vortices peculiar to the representation of the trigonal symmetry group C_{3v}. We show the emergence of a vortex carrying the winding number 2. Such a vortex is highly unusual in all branches of physics. An analytic form of wave functions makes it possible to explore deep physics of graphene nanodisks.

The inclusion of Coulomb interactions provides the ground state with a finite spin proportional to the edge length according to the following argument. Hund's rule is well known in atomic physics, according to which the ground state of atoms has the maximum spin. Thus, assuming N-fold degenerate zero-energy states, the spin of the ground state is $N/2$. On the other hand, there exists Lieb's theorem applicable to flat-band ferromagnetism, according to which the sublattice imbalance $N = |L_A - L_B|$ per unit cell leads to the polarized ground state with spin $N/2$. Both theorems are relevant to graphene nanodisks, by assuring the emergence of the polarized ground state with spin $N/2$.

The nanodisk-spin system undergoes a quasi-phase transition between the quasiferromagnet and the parramagnet(47), which is a precursor of an actual phase transition. Graphene nanodisks can be interpleted as quantum dots made of graphene, as already noticed. In this point of view, it is natural to expect Coulomb blockades(46) and Kondo effects(47) by connecting a nanodisk with leads.

On the other hand, the study of spin-dependent transport phenomena has recently attracted much attention(52; 53). It has opened the way to the field of spintronics(54–57), literally spin

electronics, where new device functionalities exploit both the charge and spin degrees of freedom. There are various approaches in this sphere. For instance, the use of a quantum-dot setup(58; 59) has been proposed, which can be operated either as a spin filter to produce spin-polarized currents or as a device to detect and manipulate spin states. However, there are difficulties of spintronics based on conventional materials, since spin directions are quickly relaxed and coherence is easily lost due to spin-orbit interactions. In graphene, spin relaxation length is as large as $2\mu m$ due to small spin-orbit interactions(60), as has been confirmed by spin precession measurement. Long spin relaxation length has motivated spintronics based on graphene(60–63) recently. Nevertheless, there exists a key issue how to generate and manipulate spin currents. Localized spins are necessary for this purpose. It can be solved by a new type of materials, graphene nanodisks. Some application to spintronics, such as a spin filter, a spin valve and a spin switch has been proposed(64–66).

This work is organized as follows. In Section 3, we summarize the basic nature of trigonal zigzag nanodisks. We introduce the size parameter N for trigonal zigzag nanodisks. There exists N-fold degenerate zero-energy states, implying that the zero-energy sector has the SU(N) symmetry. We classify them according to the representation of the trigonal symmetry group C_{3v}. In Section 4, we analyze these zero-energy states based on the Dirac theory of graphene. They are shown to be edge modes indexed by the edge momentum and grouped according to the representation of the trigonal symmetry group C_{3v}. Wave functions are explicitly constructed as analytic functions around the K point and as anti-analytic functions around the K' point. By evaluating the probability density flow we find a texture of magnetic vortices perpendicular to the nanodisk plane. It is intriguing that a vortex with the winding number 2 emerges in the state belonging to the E (doublet) representation. In Section 5, we make an investigation of electron-electron interaction effects in the zero-energy sector. We derive explicitly the direct and exchange interactions, which break the SU(N) symmetry but not so strongly. We show that the spin stiffness is quite large due to large exchange interactions, which means that a nanodisk is a rigid ferromagnet. The system is well described by the infinite-range Heisenberg model within the SU(N) approximation, which is exactly solvable. We explore thermodynamical properties. Constructing the partition function, we calculate the specific heat, the entropy, the magnetization and the susceptibility. A sharp peak emerges at a certain temperature ($T = T_c$) in the specific heat, which we interpret as a quasi-phase transition between the quasiferromagnet and quasiparamagnet states. In Section 6, we argue that our analysis based on the zero-energy sector stands as it is even if the size of the nanodisk is large. In Section 8.0.0.3, we make an investigation of the spin current, the spin-filter effects. We first analyze how the spin of a nanodisk filters the spin of the current by assuming that the nanodisk is a rigid ferromagnet. However, the nanodisk is actually not a rigid ferromagnet but a quasiferromagnet. Hence an intriguing reaction phenomenon occurs: Namely, the spin of the nanodisk can be controlled by the spin of the current. We analyze the reaction to the spin of the nanodisk from the spin of electrons in the current. In Section 8, we propose a rich variety of spintronic devices made of nanodisks and leads, such as spin memory, spin amplifier, spin valve, spin-field-effect transistor, spin diode and spin switch. Graphene nanodisks could well be basic components of future nanoelectronic and spintronic devices.

2. Sample

It is possible to manufacture graphene nanoribbon and nanodisk by etching a graphene sheet. Here we review a method to produce crystallographically oriented cuts in single-layer

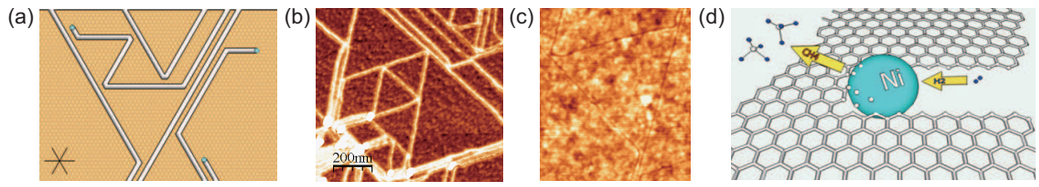

.

Fig. 2. (a) Key features of etching in SLG are chirality-preserving angles of 60 and 120, avoided crossing of trenches leaving ∼10 nm spacing between adjacent trenches and producing connected nanostructures, and trenches and nanoparticles with uniform width < 10 nm. (b) AFM phase image of etched SLG with produced geometric nanostructures. The phase image obscures small details, making adjacent trenches appear to merge together. (c) AFM height image of equilateral triangle connected to three nanoribbons. (d) artoon of a Ni particle etching a graphene sheet (not to scale). Ni nanoparticles absorb carbon from graphene edges which then reacts with H2 to create methane. These figures are taken from the work of Campos et al. (44)

graphene (SLG) which effectively has all cuts oriented with the same edge-chirality based on the work of Campos et al. (44). By using this method nanoribbons, equilateral triangles (trigonal nanodisks), and other graphene nanostructures are fabricated, which could feature novel electronic behavior resulting from their specific edge orientations.

During the high-temperature etching stage, the Ni nanoparticles etch the graphene through catalytic hydrogenation of carbon, where carbon atoms from exposed graphene edges dissociate into the Ni nanoparticle, and then react with H_2 at the Ni surface. This process is summarized by the chemical reaction

$$\mathrm{Ni} + \mathrm{C}_{\mathrm{graphene}} + 2\mathrm{H}_2 \rightarrow \mathrm{Ni} + \mathrm{CH}_4, \tag{1}$$

where carbon from the graphene is hydrogenated into methane by the Ni nanoparticle catalyst. The same reaction can also be understood as the effective reverse of catalytic carbon nanotube (CNT) growth, and indeed it is found that the growth of CNTs competes with the desired etching results in graphene. This occurs because at high concentrations of carbon the Ni nanoparticles become supersaturated with carbon and can begin to expel carbon nanotubes. It is for this reason that extra precaution is necessary during preparation to avoid organic contaminants which can act as carbon sources and saturate the Ni nanoparticles. In addition, methane produced by the etching process itself can supersaturate the Ni nanoparticles if the amount of Ni on the substrate is too low.

The etching process produces a mosaic of clearly defined cuts across the SLG surface, as measured by atomic force microscopy [Fig.2(b,c)]. These continuous trenches left behind by individual nanoparticles run along straight lines, intermittently deflecting from their path or reflecting away from previously etched trenches. These deflections and reflections show a surprising regularity, with measured angles between any pair of trenches of either 60° or 120° [Fig. 2(a)]. Trenches forming edges at angles of 60° and 120° preserve the chirality of the edges, indicating that nearly all the cuts in our samples run along the same crystallographic orientation.

3. Electronic properties of nanodisks

In this section we summarize the basic nature of trigonal zigzag nanodisks(36). There exists N-fold degenerate zero-energy states, implying that the zero-energy sector has the SU(N)

symmetry. All these states are classified into singlets (A representation) and doublets (E representation) according to the representation of the trigonal symmetry group C_{3v}. Wave functions are constructed explicitly by diagonalizing the Hamiltonian.

3.1 Classification of nanodisks

We first explore the electronic and magnetic properties of graphene nanodisks. It is a nanometer-scale disk-like graphene derivative which has a closed edge. There are many type of nanodisks, where typical examples are displayed in Fig.1. Graphene nanodisks are classified by the edge and shape. Typical edges are zigzag edge and armchair edge, while typical shapes are trigonal shape and hexagonal shape.

3.2 Energy Spectrum of nanodisks

We calculate the energy spectra of graphene derivatives based on the nearest-neighbor tight-binding model, which has been successfully applied to the studies of carbon nanotubes and graphene nanoribbons. The Hamiltonian is given by

$$H = \sum_i \varepsilon_i c^\dagger_{i,\sigma} c_{i,\sigma} + \sum_{\langle i,j \rangle} t_{ij} c^\dagger_{i,\sigma} c_{j,\sigma}, \tag{2}$$

where ε_i is the site energy, t_{ij} is the transfer energy, and $c^\dagger_{i,\sigma}$ is the creation operator of the π electron with spin σ at site i. The sum is taken over all nearest-neighboring sites $\langle i, j \rangle$. Owing to their homogeneous geometrical configuration, we may take constant values for these energies, $\varepsilon_i = \varepsilon_{\rm F}$ (Fermi energy) and $t_{ij} = t \approx 2.70$eV. Then, the diagonal term in (2) yields just a constant, $\varepsilon_{\rm F} N_{\rm C}$, where $N_{\rm C}$ is the number of carbon atoms in the system. The Hamiltonian (2) yields the Weyl electrons for graphene(12; 13; 67), as we review in Section 4.1. There exists one electron per one carbon and thus the band-filling factor is 1/2. It is customarily chosen as the zero-energy level of the tight-binding Hamiltonian (2) at this point so that the energy spectrum is symmetric between the positive and negative energy states. Therefore, the system is metallic provided that there exists zero-energy states in the spectrum. It is understood that carbon atoms at edges are terminated by hydrogen atoms. We carry out the calculation together with this condition.

In analyzing a nanodisk containing $N_{\rm C}$ carbon atoms, the Hamiltonian (2) is reduced to an $N_{\rm C} \times N_{\rm C}$ matrix. It is possible to exactly diagonalize the Hamiltonian to determine the energy spectrum E_i together with its degeneracy g_i for each nanodisk. The density of state is given by

$$D(\varepsilon) = \sum_{i=1}^{N_{\rm C}} g_i \delta(\varepsilon - E_i). \tag{3}$$

We have explicitly diagonalized the Hamiltonian (2) for several nanodisks with trigonal zigzag shape, trigonal armchair shape and hexagonal zigzag shape. It is remarkable that there exist zero-energy states only in trigonal zigzag nanodisks. We have also checked explicitly the absence of the zero-energy state in a series of nanodisks with hexagonal armchair type. Actually there exist general arguments for the number of zero-energy states: See Section 3.4.2 with the use of the electron-hole symmetry and Section 3.4.4 with the use of the graph theory. We comment on the validity of the tight-binding model. Although the model may be viewed as too naive, it actually gives quite good results in the graphene system for the following reasons. First, the graphene is composed of a single kind of atoms, namely, carbons. It is a "super-clean material", as is the He liquid. Accuracy of the tight-binding model increases

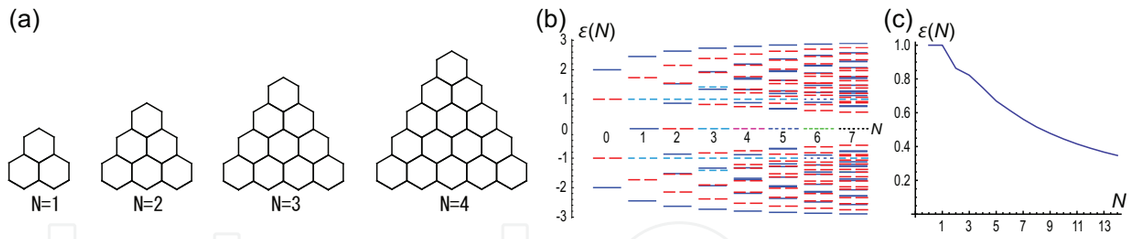

Fig. 3. (a) Geometric configuration of trigonal zigzag nanodisks. We define its size N by $N = N_{\rm ben} - 1$ with $N_{\rm ben}$ the number of benzenes on one side of the trigon. Here, $N = 1, 2, 3, 4, 5$. The number of carbon atoms are related as $N_{\rm C} = N^2 + 6N + 6$. (b) Density of states of the N-trigonal nanodisk for $N = 0, 1, 2, \cdots, 7$. The horizontal axis is the size N and the vertical axis is the energy $\varepsilon(N)$ in units of $t = 2.7$eV. Segments in each energy level indicate the degeneracy of the level. (c) The excitation gap ε as a function of the size N. It is approximately proportional to N^{-1}.

as the number of involved elements becomes lower. For instance, it is hard to determine the energy spectrum by the simple tight-binding model in transition metal oxides, since it contains many elements. Second, carbon is a light element, and there are only a few electrons in the shell. Especially in carbon there are only s and p orbitals. Furthermore, it is possible to neglect spin-orbit couplings since they are very small. Third, the graphene consists of the sp^2 orbital and the π orbital, where sp^2 orbitals contribute to make a rigid skeleton of the graphene structure, while π orbitals spread out in graphene and behave as free electrons. These two energy levels are well separated. Consequently, the simple tight-binding Hamiltonian presents a very good description of the graphene system by treating π electrons as free electrons.

3.3 Trigonal zigzag nanodisks

We shall investigate trigonal zigzag nanodisks in more details since they have zero-energy states. We define the size N of a nanodisk by $N = N_{\rm ben} - 1$, where $N_{\rm ben}$ is the number of benzenes on one side of the trigon as in Fig.3(a). We show the density of state for $N = 1, 2, \cdots, 5$ in Fig.3(b).

It can be shown that the determinant associated with the Hamiltonian (2) has such a factor as

$$\det\left[\varepsilon I - H\left(N_{\rm C}\right)\right] \propto \varepsilon^N, \tag{4}$$

implying N-fold degeneracy of the zero-energy states. Since there exist half-filled zero-energy states for $N \geq 1$, these nanodisks are "metallic". The gap energy between the first-excitation and the ground states decreases as the size becomes larger [Fig.3(c)].

3.4 Zero-energy sector

The size-N nanodisk has N-fold degenerate zero-energy states, where the gap energy is as large as a few eV. Hence it is a good approximation to investigate the electron-electron interaction physics only in the zero-energy sector, by projecting the system to the subspace made of those zero-energy states. The zero-energy sector consists of N orthonormal states $|f_\alpha\rangle$, $\alpha = 1, 2, \cdots, N$, together with the SU(N) symmetry. We can expand the wave function of the state $|f_\alpha\rangle$ as

$$f_\alpha(\boldsymbol{x}) = \sum_i \omega_i^\alpha \varphi_i(\boldsymbol{x}), \tag{5}$$

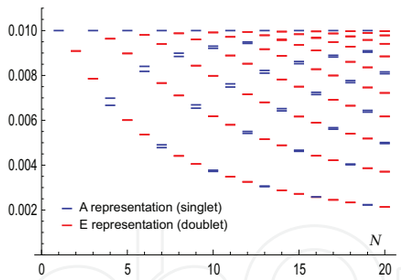

Fig. 4. Zero-energy states split into several nonzero-energy states by edge modifications. The horizontal axis is size N and the vertical axis is energy in units of $t = 2.7$eV. We take $\varepsilon_i = \varepsilon + \Delta\varepsilon$ for all edge carbons with $\Delta\varepsilon = 0.027$eV. States are grouped according to the representation of the trigonal symmetry C_{3V}. Doublet states (red) obey the E representation. Singlet states (blue) appear in pairs; the upper (lower) states obey the A_1 (A_2) representation.

where $\varphi_i(\boldsymbol{x})$ is the Wannier function localized at the site i. The operator c_i in the tight-binding Hamiltonian (2) annihilates an electron in the state described by the Wannier function $\varphi_i(\boldsymbol{x})$.

3.4.1 Trigonal symmetry

We are able to calculate the amplitude ω_i for zero-energy states in the trigonal zigzag nanodisk. In so doing it is necessary to select the N orthonormal states $|f_\alpha\rangle$ according to the representation theory of group. The symmetry group of the trigonal nanodisk is C_{3v}, which is generated by the $2\pi/3$ rotation $\mathfrak{c}_3$ and the mirror reflection $\sigma_\mathfrak{v}$. It has the representation $\{A_1, A_2, E\}$. The A_1 representation is invariant under the rotation $\mathfrak{c}_3$ and the mirror reflection $\sigma_\mathfrak{v}$. The A_2 representation is invariant under $\mathfrak{c}_3$ and antisymmetric under $\sigma_\mathfrak{v}$. The E representation acquires $\pm 2\pi/3$ phase shift under the $2\pi/3$ rotation. The A_1 and A_2 are 1-dimensional representations (singlets) and the E is a 2-dimensitional representation (doublet). These properties are summarized in the following character table:

C_{3v}	$\mathfrak{e}$	$2\mathfrak{c}_3$	$3\sigma_\mathfrak{v}$
A_1	1	1	1
A_2	1	1	-1
E	2	-1	0

(6)

The N orthonormal states $|f_\alpha\rangle$ together with the amplitude ω_i are constructed as follows. First, by requiring the mirror symmetry, we can explicitly construct the wave functions, all of which are found to be real. Next, we make appropriate linear combinations of these states to satisfy the trigonal symmetry C_{3v}. For this purpose, we resolve the degeneracy by applying C_{3v}-invariant perturbation to the size-N trigonal nanodisk. We note that all their wave functions are nonvanishing on edge sites and that they penetrate into the bulk with different penetration depth. Hence, if we apply an identical bias voltage to all edge carbons, we expect that the energy of the mode increases, as the penetration depth decreases. We take $\varepsilon_i = \varepsilon + \Delta\varepsilon$ for all edge carbons. We show how the zero-energy states split by taking $\Delta\varepsilon = 0.01t = 0.027$eV in Fig.4 for $N = 1, 2, \cdots, 20$. All zero-energy states are found to acquire positive energy and they become singlets or doublets. Singlet states obey the A_1 or A_2 representation, while appropriate linear combinatations of doublet states obey the E representation. There exists a nondegenerate state which has the highest energy for a nanodisk with $N =$odd, which is argued to belong A_2 representation. There are no such wave functions for nanodisks with $N =$even.

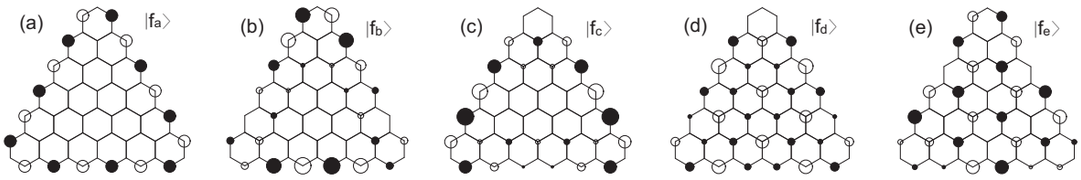

Fig. 5. (a)∼(e) The zero-energy states of the trigonal nanodisk with size $N = 5$. They are symmetric under the mirror reflection with respect to the vertical axis. The solid (open) circle denotes the positive (negative) amplitude ω_i. The amplitude is proportional to the radius of circle. Electrons are localized on edges in the state (a). When the site energy ε_i is increased at edges equally, the degeneracy is partially resolved, as illustrated in Fig.4. The state (a) has the highest energy and is a singlet in the A_2 representation of the symmetry group C_{v3}. The states (b) and (c) are degenerate; the states (d) and (e) are degenerate and have the lowest energy.

Let us explain the above scheme by taking an example of the nanodisk with size $N = 5$. First, we present 5 orthonormal states $|f_\alpha\rangle$ in Fig.5, where the solid (open) circle denotes the positive (negative) amplitude ω_i with $|\omega_i|$ being proportional to the radius of the circle. Second, the wave function $|f_{\rm a}\rangle$ is entirely localized on edge sites as in Fig.5(a). Since it is invariant under the $2\pi/3$ rotation $\mathfrak{c}_3$ and antisymmetric under the mirror reflection $\sigma_{\mathfrak{v}}$, it is a singlet state obeying the A_2 representation. Third, we find two sets of states $(|f_b\rangle, |f_c\rangle)$ and $(|f_d\rangle, |f_e\rangle)$ are degenerate under the C_{3v}-invariant perturbation. Thus, we have identified 5 states in the spectrum of Fig.4. From the mirror symmetric states we construct the trigonal symmetric states by making a linear combination within each doublet, $|g_\pm\rangle = \frac{1}{\sqrt{2}}(|f_b\rangle \pm i|f_c\rangle)$, $|h_\pm\rangle = \frac{1}{\sqrt{2}}(|f_d\rangle \pm i|f_e\rangle)$. Each sets of complex wave functions, $(|g_+\rangle, |g_-\rangle)$ and $(|h_+\rangle, |h_-\rangle)$, transform properly under the E representation. We shall present an analytic approach to investigate these states based on the Dirac theory in Section 4.3. In the instance of $N = 5$, $(|g_+\rangle, |g_-\rangle)$ and $(|h_+\rangle, |h_-\rangle)$ correspond to $(|+k_2^+\rangle, |-k_2^+\rangle)$ and $(|+k_2^-\rangle, |-k_2^-\rangle)$, respectively, with $k_n^\pm$ being defined in (38).

3.4.2 Electron-hole symmetry

We have shown that the zero-energy sector of the trigonal zigzag nanodisk has the N-fold degeneracy by diagonalizing the Hamiltonian (2) explicitly. We wish to derive this fact from a general point of view. First, we appeal to the electron-hole symmetry of the tight-binding Hamiltonian (2). The Hamiltonian is invariant under the electron-hole transformation, $c_{\sigma,A} \to c_{\sigma,A}^\dagger$, $c_{\sigma,B} \to -c_{\sigma,B}^\dagger$. As a result, the band structure is symmetric between the positive-energy states and the negative-energy states, as is explicitly seen in Fig.3(b). The number of the positive-energy state ν_+ and the negative-energy state ν_- are equal $\nu_+ = \nu_-$. On the other hand, the number of the total states is equal to the number of carbon atoms, $N_{\rm C} = N^2 + 6N + 6$. Hence, the number of the zero-enegy state η is given by $\eta = N_{\rm C} - \nu_+ - \nu_-$. Now, the number of the positive or negative-energy state is less than $2\min[N_A, N_B]$, $\nu_\pm \le 2\min[N_A, N_B]$, where N_A and N_B are the numbers of sites in sublattices A and B, respectively [see Fig.6]. We obtain $\eta \ge |N_A - N_B|$. It is easy to see $N_A = (N+1)(N+6)/2$, $N_B = (N+2)(N+3)/2$ for the trigonal zigzag nanodisk, and hence $\eta \ge N$ for the size-N nanodisk.

3.4.3 Bipartite lattice

We have derived the lower limit for the dimension of the zero-energy sector, $\eta \ge N$. It is a characteristic feature of the tight-binding Hamiltonian on the bipartite lattice that it can be

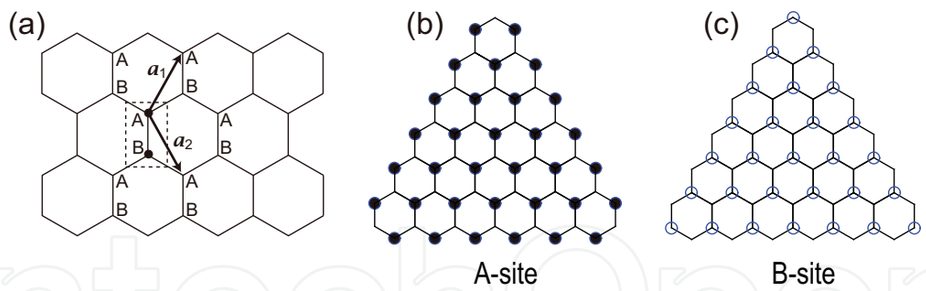

Fig. 6. (a) The two-dimensional honeycomb lattice is made of two trigonal sublattices generated by the two basis vectors $\boldsymbol{a}_1$ and $\boldsymbol{a}_2$ from the two base points A and B in primitive cell (dotted rectangle). (b,c) The A-sites and B-sites of a trigonal nanodisk. Electrons exist only in A sites.

represented in the form of

$$H = \begin{pmatrix} 0 & T_{AB} \\ T_{BA} & 0 \end{pmatrix}. \tag{7}$$

The wave function is decomposed into two parts describing the A sites and B sites, $|f\rangle = (f_A, f_B)^t$. The rank of the matrix (7) is $2N_B$ at the highest, but it is $2N_B$ for connected lattices. As a result the number of the zero-energy eigenvalues of the $(N_A + N_B)$-dimensional matrix (7) is given by $\eta = N_A - N_B = N$, where the last equality holds for the zigzag trigonal nanodisk with (**??**).

Furthermore, we are able to show that the wave function takes a nonzero value only on the A-site. The matrix T_{BA} is $N_B \times N_A$ dimensional. Let us choose N_A-dimensional eigenvectors satisfying $T_{BA}|f_A\rangle = 0$. The number of such eigenvectors is $N = N_A - N_B > 0$, as we have just shown. We now consider the $(N_A + N_B)$-dimensional vector, $|f_A\rangle = (f_A, 0)^t$. It is trivial to see that it is the eigenvector of H, $H|f_A\rangle = (0, T_{BA}f_A)^t = 0$. We have proved that there are N zero-energy eigenvalues whose wave functions vanish on all B sites. See Fig.5 and Fig.6.

3.4.4 Graph theory

There is another way to see the dimension of the zero-energy sector. The spectrum of the tight binding Hamiltonian of a honeycomb system can also be analyzed on the basis of a mathematically rigorous approach of the benzenoid graph theory(68). According to this graph theory, the number of zero-energy states is equal to the graph's nullity, $\eta = 2\alpha - N_C$, where N_C is the total number of sites and α is the maximum number of non-adjacent sites. Here, we have $\eta = N$, since $\alpha = N_A$ for the trigonal zigzag nanodisk [Fig.6].

3.5 Robustness against randomness and lattice defects

In actual application, however, it is important to discuss how stable the previous results are against lattice defects and randomness in transfer energy. We study three types of randomness: randomness in transfer energy, randomness in site energy and lattice defects. The modified Hamiltonian is

$$H_0 = \sum_i (\varepsilon_i + \delta\varepsilon_i)\, c^\dagger_{i,\sigma} c_{i,\sigma} + \sum_{\langle i,j \rangle} \left(t_{ij} + \delta t_{ij}\right) c^\dagger_{i,\sigma} c_{j,\sigma}, \tag{8}$$

where we take random values for $\delta\varepsilon_i$ and δt_{ij}.

First of all the total spin of the ground state is determined by Lieb's theorem although transfer randomness and lattice defects are included. (See Section 5.5 for Lieb's theorem.) The total

Fig. 7. Energy level with randomness. (a) Clean nanodisks. (b) Site energy randomness, $\delta\varepsilon_i/t \sim \pm 0.1$. (c) Transfer energy randomness, $\delta t_{ij}/t \sim \pm 0.1$. (d) Lattice defects with thre site at a corner. See Fig.8(a).

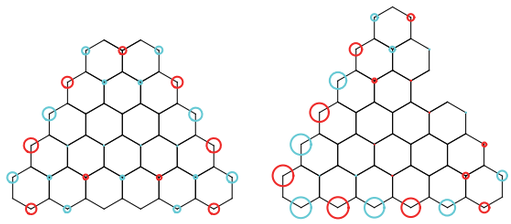

Fig. 8. Wave function with lattice defects. (a) Three atoms are absent at one corner. (b) One atom is absent at one edge. For both case the probability density drastically reduces near the lattice defects. The number of the zero-energy states reduces from N to $N-1$ for both cases.

spin is given by the difference of the A site and the B site, $S = \frac{1}{2}|N_A - N_B - \delta_A + \delta_B|$, with the number of lattice defects at A (B) site δ_A (δ_B), where N_A and N_B are number of A site and B site without lattice defects. The total spin does not change by introducing randomness in transfer energies. On the other hand, the number of the zero-energy states changes by the number of lattice defects. When site randomness is included, we can not resort to Lieb's theorem in the strict sense because the lattice is no longer bipertite. However, when the split due to the site randomness is smaller than that due to the Coulomb interaction, the total spin does not change.

We show the energy spectrum with the randomness in Fig.7, where we have taken rather large random values for $\delta\varepsilon_i$ and δt_{ij}: We have generated uniform random numbers in the region $|\delta\varepsilon_i|/t \leq \pm 0.1$ and $|\delta t_{ij}|/t \leq \pm 0.1$. The zero energy remains as it is even when we introduce lattice defects. However the zero-energy states split by the randomness in transfer energy. The wave functions also change by the lattice defect and the randomness in site and transfer energies. The changes are proportional to the site (transfer) modification $\delta\varepsilon_i$ (δt_{ij}), but slight in site and transfer randomness.

On the other hand, the wave functions drastically change by introducing lattice defects, as shown in Fig.8. We find the density reduces drastically near the lattice defects.

4. Dirac electrons in graphene

In this section we analyze the zero-energy states based on the Dirac theory of graphene(48). We explicitly construct wave functions as analytic functions around the K point and as anti-analytic functions around the K' point. They are indexed by the edge momentum and grouped according to the representation of the trigonal symmetry group C_{3v}. By evaluating the probability density flow we reveal a novel texture of magnetic vortices perpendicular to

the nanodisk plane. It is intriguing that a vortex with the winding number 2 emerges in the state belonging to the E (doublet) representation.

4.1 Weyl equations

Electrons obey the massless two-component Dirac equation, or the Weyl equation, in graphene(49–51). We start with a review how Dirac electrons arise from the one-particle electronic states in the honeycomb lattice [Fig.9]. We take the basis vectors $\boldsymbol{a}_1$ and $\boldsymbol{a}_2$ as $\boldsymbol{a}_1 = (1,0)\,a$, $\boldsymbol{a}_2 = \left(1/2, \sqrt{3}/2\right) a$, with a the lattice constant ($a \approx 2.46$Å). The honeycomb lattice has two different atoms per primitive cell, which we call the A and B sites. There are three B sites adjacent to an A site, which are specified by the three vectors $\boldsymbol{r}_i$ with $\boldsymbol{r}_1 = \left(0, -1/\sqrt{3}\right) a$, $\boldsymbol{r}_2 = \left(1/2, 1/\left(2\sqrt{3}\right)\right) a$, $\boldsymbol{r}_3 = \left(-1/2, 1/\left(2\sqrt{3}\right)\right) a$. The basis vectors $\boldsymbol{b}_i$ of the reciprocal lattice are given by solving the relations $\boldsymbol{b}_i \cdot \boldsymbol{a}_j = 2\pi\delta_{ij}$. The Brillouin zone is a hexagon in the reciprocal lattice with opposite sides identified.
We rewrite the tight-binding Hamiltonian (2) as

$$H = t \sum_{\boldsymbol{x},i} \left[c_{\mathrm{A}}^{\dagger}(\boldsymbol{x})\, c_{\mathrm{B}}(\boldsymbol{x} + \boldsymbol{r}_i) + c_{\mathrm{B}}^{\dagger}(\boldsymbol{x} + \boldsymbol{r}_i)\, c_{\mathrm{A}}(\boldsymbol{x}) \right], \tag{9}$$

where c_S and $c_S^{\dagger}$ are the annihilation and creation operators for electrons localized at the S site (S =A,B). It describes a transfer of an electron between neighboring A and B sites without changing its spin. We introduce the Fourier transform of the electron annihilation operator $c_S(\boldsymbol{x})$,

$$c_S(\boldsymbol{x}) = \int \frac{d^2k}{2\pi} e^{i\boldsymbol{k}\cdot\boldsymbol{x}} c_S(\boldsymbol{k}). \tag{10}$$

The Hamiltonian (9) reads

$$H = t \int d^2k \left(c_{\mathrm{A}}^{\dagger}, c_{\mathrm{B}}^{\dagger} \right) \begin{pmatrix} 0 & f(\boldsymbol{k}) \\ f^*(\boldsymbol{k}) & 0 \end{pmatrix} \begin{pmatrix} c_{\mathrm{A}} \\ c_{\mathrm{B}} \end{pmatrix} \tag{11}$$

in the momentum space, where

$$f(\boldsymbol{k}) = e^{-ik_y a/\sqrt{3}} + 2e^{ik_y a/2\sqrt{3}} \cos\frac{k_x a}{2}. \tag{12}$$

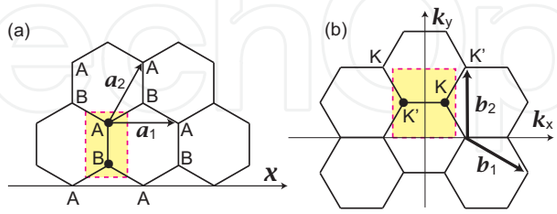

Fig. 9. (a) The two-dimensional honeycomb lattice is made of two triangular sublattices generated by the two basis vectors $\boldsymbol{a}_1$ and $\boldsymbol{a}_2$ from the base points A and B in a primitive cell (a dotted rectangle in yellow). (b) The reciplocal lattice is also a honeycomb lattice with the basis vectors $\boldsymbol{b}_1$ and $\boldsymbol{b}_2$. We take the Brillouin zone as indicated by a dotted rectangle in yellow. As two inequivalent points we take K and K′ as indicated.

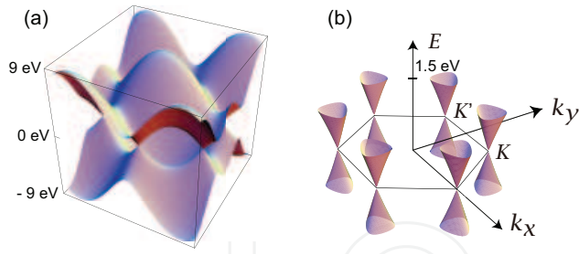

Fig. 10. (a) The overall valley structure of the dispersion relation (13) is illustrated. (b) A schematic diagram of the low-energy dispersion relation (13) near the Dirac points (K and K′ points) in the Brillouin zone. Only two Dirac cones are inequivalent to one another.

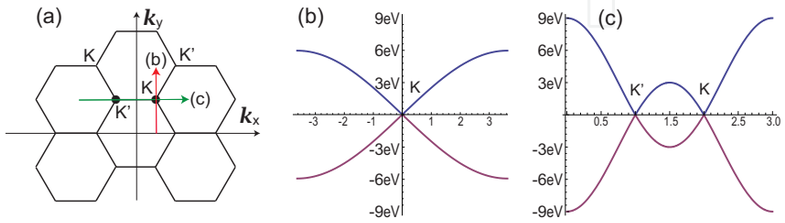

Fig. 11. Linear dispersion near the Brillouin zone corner. The linear region of the band is found to be dependent on the direction in the $\boldsymbol{k}$ space. In one of the direction (c) the linearity is good more than 3 eV.

The eigenvalues are found to be $\pm E\left(\boldsymbol{k}\right)$ with

$$E\left(\boldsymbol{k}\right)=t\sqrt{1+4\cos\frac{\sqrt{3}k_{y}a}{2}\cos\frac{k_{x}a}{2}+4\cos^{2}\frac{k_{x}a}{2}}. \tag{13}$$

The dispersion relation (13) implies that the Fermi level at $E\left(\boldsymbol{k}\right)=0$ is reached by six corners of the first Brillouin zone, among which there are only two inequivalent points due to the periodicity of the reciprocal lattice. We take them as

$$\boldsymbol{K}^{+}=\left(2\pi/3,2\pi/\sqrt{3}\right)/a,\qquad \boldsymbol{K}^{-}=\left(-2\pi/3,2\pi/\sqrt{3}\right)/a, \tag{14}$$

and call them the K and K′ points [Fig.9(b) and Fig.10]. They endow graphene with a two-component structure, corresponding to two independent Fermi points. It is notable that the dispersion relation (13) has a valley structure around the K and K′ points.
The band dispersion (13) is linear in these Dirac valleys [Fig.10],

$$E_{\kappa}\left(\boldsymbol{k}\right)=\hbar v_{\mathrm{F}}|\boldsymbol{k}-\boldsymbol{K}^{\tau}|\qquad \text{for}\quad \boldsymbol{k}\simeq\boldsymbol{K}^{\tau}, \tag{15}$$

where $\tau=\pm$ is the valley index and $v_{\mathrm{F}}=\sqrt{3}ta/\left(2\hbar\right)$ is the Fermi velocity. We show two sections of the band in Fig.11, where the linear region of the band is found to be dependent on the direction in the $\boldsymbol{k}$ space. In one of the section the linearity prevails more than 3 eV, as in Fig.11(c). This linear behavior has been confirmed experimentally(69) up to 3eV.
We may expand $f(\boldsymbol{x})$ as

$$f(\boldsymbol{x})\simeq\frac{(-1)^{-1/3}\sqrt{3}}{2}\left[\tau\left(k_{x}-K^{\tau}\right)-i\left(k_{y}-K^{\tau}\right)\right] \tag{16}$$

for $\boldsymbol{k} \simeq \boldsymbol{K}^\tau$. It is convenient to introduce the reduced wave number $\hat{\boldsymbol{k}}$ by

$$\boldsymbol{k} = \boldsymbol{K}^\tau + \hat{\boldsymbol{k}}, \tag{17}$$

and rewrite the dispersion relation as

$$E(\hat{k}_x, \hat{k}_y) = \hbar v_{\mathrm{F}} \sqrt{\hat{k}_x^2 + \hat{k}_y^2} \tag{18}$$

near the K and K′ points.
It is clear from the dispersion relation illustrated in Fig.10 that the contribution to low-energy physics comes only from the regions around the two Fermi points, $\boldsymbol{k} \simeq \boldsymbol{K}^\tau$. We make the change of variable as in (17), and express the wave function $\psi_S^\tau(\boldsymbol{x})$ near the Fermi point $\boldsymbol{k} \simeq \boldsymbol{K}^\tau$ as

$$\psi_S^\tau(\boldsymbol{x}) = e^{i\boldsymbol{K}^\tau \cdot \boldsymbol{x}} \phi_S^\tau(\boldsymbol{x}), \tag{19}$$

where $\phi_S^\tau(\boldsymbol{x})$ is called the envelope function.
The dispersion relation (18) is that of 'relativistic' Dirac fermions. Indeed, we rewrite the Hamiltonian (11) as

$$\begin{aligned} H = \hbar v_{\mathrm{F}} \int d^2\hat{k} \left(c_{\mathrm{A}}^{\mathrm{K}\dagger}, c_{\mathrm{B}}^{\mathrm{K}\dagger} \right) \begin{pmatrix} 0 & \hat{k}_x - i\hat{k}_y \\ \hat{k}_x + i\hat{k}_y & 0 \end{pmatrix} \begin{pmatrix} c_{\mathrm{A}}^{\mathrm{K}} \\ c_{\mathrm{B}}^{\mathrm{K}} \end{pmatrix} \\ + \hbar v_{\mathrm{F}} \int d^2\hat{k} \left(c_{\mathrm{A}}^{\mathrm{K}'\dagger}, c_{\mathrm{B}}^{\mathrm{K}'\dagger} \right) \begin{pmatrix} 0 & -\hat{k}_x - i\hat{k}_y \\ -\hat{k}_x + i\hat{k}_y & 0 \end{pmatrix} \begin{pmatrix} c_{\mathrm{A}}^{\mathrm{K}'} \\ c_{\mathrm{B}}^{\mathrm{K}'} \end{pmatrix}, \end{aligned} \tag{20}$$

where c_S^τ is the annihilation operator for an electron at site S in the Dirac valley $\tau\,(= K, K')$. The quantum-mechanical Hamiltonian consists of two parts, $H = H^{\mathrm{K}} + H^{\mathrm{K}'}$, where

$$H^\tau = v_{\mathrm{F}}(\tau\sigma_x p_x + \sigma_y p_y) = v_{\mathrm{F}} \boldsymbol{\sigma} \cdot \boldsymbol{p}^\tau, \tag{21}$$

with $\boldsymbol{p}^\tau = (\tau p_x, p_y) = -i\hbar(\tau\partial_x, \partial_y)$. The Hamiltonian acts on the two-component envelope function,

$$\Phi^\tau(\boldsymbol{x}) = (\phi_{\mathrm{A}}^\tau(\boldsymbol{x}), \phi_{\mathrm{B}}^\tau(\boldsymbol{x}))^t. \tag{22}$$

The Weyl equations read

$$i\hbar\partial_t \Phi^\tau(\boldsymbol{x}) = v_{\mathrm{F}} \boldsymbol{\sigma} \cdot \boldsymbol{p}^\tau \Phi^\tau(\boldsymbol{x}). \tag{23}$$

Each Hamiltonian describes the two-component massless Dirac fermion, or the Weyl fermion. The symmetries of the system are as follows. First, we note that $H^{\mathrm{K}'} = \sigma_y H^{\mathrm{K}} \sigma_y$, where σ_y is the generator of the mirror symmetry. It transforms the K point into the K′ point. Next, $\sigma_z H^{\mathrm{K}} \sigma_z = -H^{\mathrm{K}}$, and $\sigma_z H^{\mathrm{K}'} \sigma_z = -H^{\mathrm{K}'}$, where σ_z is the generator of the electron-hole symmetry. It transforms the positive-energy state into the negative-energy state.
Eigenfunctions of the Hamiltonian (21) are readily obtained,

$$\Phi_\pm^\tau(\boldsymbol{x}) = e^{i\hat{\boldsymbol{k}} \cdot \boldsymbol{x}} u_\pm^\tau(\hat{\boldsymbol{k}}) \tag{24}$$

for the positive-energy state $\Phi_+^\tau(\boldsymbol{x})$ and the negative-energy state $\Phi_-^\tau(\boldsymbol{x})$, where

$$u_\pm^{\mathrm{K}}(\hat{\boldsymbol{k}}) = \frac{1}{\sqrt{2}} \left(1 \pm \frac{\boldsymbol{\sigma} \cdot \hat{\boldsymbol{k}}}{|\boldsymbol{k}|} \right) \begin{pmatrix} 1 \\ 0 \end{pmatrix}, \quad u_\pm^{\mathrm{K}'}(\hat{\boldsymbol{k}}) = \frac{1}{\sqrt{2}} \left(1 \pm \frac{\boldsymbol{\sigma} \cdot \hat{\boldsymbol{k}}'}{|\boldsymbol{k}'|} \right) \begin{pmatrix} 0 \\ 1 \end{pmatrix}, \tag{25}$$

with $\hat{\boldsymbol{k}}' = (-\hat{\boldsymbol{k}}_x, \hat{\boldsymbol{k}}_y)$. They transform as

$$\sigma_y u_{\pm}^{\mathrm{K}}(\hat{\boldsymbol{k}}) = i u_{\pm}^{\mathrm{K}'}(\hat{\boldsymbol{k}}), \quad \sigma_y u_{\pm}^{\mathrm{K}'}(\hat{\boldsymbol{k}}) = -i u_{\pm}^{\mathrm{K}}(\hat{\boldsymbol{k}}), \quad \sigma_z u_{\pm}^{\mathrm{K}}(\hat{\boldsymbol{k}}) = u_{\mp}^{\mathrm{K}}(\hat{\boldsymbol{k}}), \quad \sigma_z u_{\pm}^{\mathrm{K}'}(\hat{\boldsymbol{k}}) = -u_{\mp}^{\mathrm{K}'}(\hat{\boldsymbol{k}}), \tag{26}$$

under the mirror transformation and the electron-hole transformation.
The energy spectrum is symmetric between positive- and negative-energy states. There exists one electron per one carbon and the band-filling factor is $1/2$ in graphene. Namely, all negative-energy states are filled up, as is a reminiscence of the Dirac sea.

4.2 Dirac electrons on zigzag edge

We analyze massless Dirac electrons on the zigzag edge based on the method due to Brey and Fertig(22). The Weyl equation holds for envelope functions satsifying

$$v_{\mathrm{F}} \begin{pmatrix} 0 & \tau p_x - i p_y \\ \tau p_x + i p_y & 0 \end{pmatrix} \begin{pmatrix} \phi_{\mathrm{A}}^{\mathrm{K}^\tau}(\boldsymbol{x}) \\ \phi_{\mathrm{B}}^{\mathrm{K}^\tau}(\boldsymbol{x}) \end{pmatrix} = E \begin{pmatrix} \phi_{\mathrm{A}}^{\mathrm{K}^\tau}(\boldsymbol{x}) \\ \phi_{\mathrm{B}}^{\mathrm{K}^\tau}(\boldsymbol{x}) \end{pmatrix}, \tag{27a}$$

where $p_x - i p_y = -2i\hbar\partial_z$, $p_x + i p_y = -2i\hbar\partial_{z^*}$ with $z = x + iy$ and $z^* = x - iy$. The Weyl equation is rewritten as

$$\partial_{z^*}\phi_{\mathrm{A}}^{\mathrm{K}}(\boldsymbol{x}) = i\frac{E}{2\hbar v_{\mathrm{F}}}\phi_{\mathrm{B}}^{\mathrm{K}}(\boldsymbol{x}), \qquad \partial_z \phi_{\mathrm{B}}^{\mathrm{K}}(\boldsymbol{x}) = i\frac{E}{2\hbar v_{\mathrm{F}}}\phi_{\mathrm{A}}^{\mathrm{K}}(\boldsymbol{x}), \tag{28a}$$

$$\partial_z \phi_{\mathrm{A}}^{\mathrm{K}'}(\boldsymbol{x}) = -i\frac{E}{2\hbar v_{\mathrm{F}}}\phi_{\mathrm{B}}^{\mathrm{K}'}(\boldsymbol{x}), \qquad \partial_{z^*}\phi_{\mathrm{B}}^{\mathrm{K}'}(\boldsymbol{x}) = -i\frac{E}{2\hbar v_{\mathrm{F}}}\phi_{\mathrm{A}}^{\mathrm{K}'}(\boldsymbol{x}). \tag{28b}$$

It is clear that, for the zero-energy state ($E = 0$), the envelope functions $\phi_{\mathrm{A}}^{\mathrm{K}}(\boldsymbol{x})$ and $\phi_{\mathrm{B}}^{\mathrm{K}'}(\boldsymbol{x})$ are analytic, while $\phi_{\mathrm{B}}^{\mathrm{K}}(\boldsymbol{x})$ and $\phi_{\mathrm{A}}^{\mathrm{K}'}(\boldsymbol{x})$ are anti-analytic.
We place a graphene sheet in the upper half plane ($y > 0$) with the edge at $y = 0$. Translational invariance in the x direction dictates the envelope functions are of the form $\phi_S^\tau(x, y) = e^{i\hat{k}_x x} f_S^\tau(y)$. Analyticity requirement allows us to write

$$\phi_{\mathrm{A}}^{\mathrm{K}}(\boldsymbol{x}) = C_{\mathrm{A}}^{\mathrm{K}} e^{i\hat{k}z}, \quad \phi_{\mathrm{B}}^{\mathrm{K}}(\boldsymbol{x}) = C_{\mathrm{B}}^{\mathrm{K}} e^{i\hat{k}z^*}, \quad \phi_{\mathrm{A}}^{\mathrm{K}'}(\boldsymbol{x}) = C_{\mathrm{A}}^{\mathrm{K}'} e^{i\hat{k}z^*}, \quad \phi_{\mathrm{B}}^{\mathrm{K}'}(\boldsymbol{x}) = C_{\mathrm{B}}^{\mathrm{K}'} e^{i\hat{k}z}, \tag{29a}$$

with C_S^τ being integration constant.
According to the tight-binding-model result, there are no electrons in the B site on edges with zero energy, and hence we require

$$\phi_{\mathrm{B}}^{\mathrm{K}}(y = 0) = \phi_{\mathrm{B}}^{\mathrm{K}'}(y = 0) = 0. \tag{30}$$

By avoiding divergence at $y \to \infty$, the resultant envelope functions are found to be

$$\phi_{\mathrm{A}}^{\mathrm{K}}(\boldsymbol{x}) = \sqrt{\hat{k}/L} e^{i\hat{k}z} = \sqrt{\hat{k}/L} e^{i\hat{k}x - \hat{k}y}, \quad \text{for} \quad \hat{k} > 0, \tag{31a}$$

$$\phi_{\mathrm{A}}^{\mathrm{K}'}(\boldsymbol{x}) = \sqrt{\hat{k}/L} e^{i\hat{k}z^*} = \sqrt{\hat{k}/L} e^{i\hat{k}x - |\hat{k}|y}, \quad \text{for} \quad \hat{k} < 0, \tag{31b}$$

with all other components being zero, where $2L$ is the size of the edge.
The wave number is a continuous parameter for an infinitely long graphene edge. According to the tight-binding-model result, as illustrated in Fig.13, the flat band emerges for

$$-\pi \le ak < -\frac{2\pi}{3} \quad \text{and} \quad \frac{2\pi}{3} < ak \le \pi, \tag{32}$$

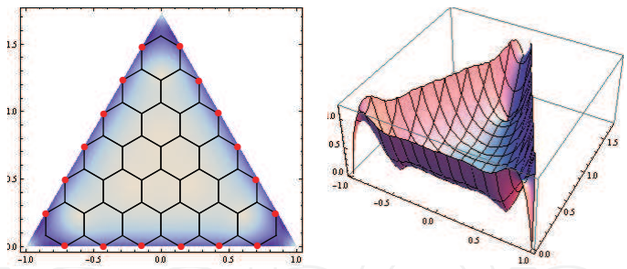

Fig. 12. The electron density is found to be localized along the edges of a trigonal nanodisk.

in terms of the original wave number k, or

$$-\frac{\pi}{3} \leq a\hat{k} < 0 \quad \text{and} \quad 0 < a\hat{k} \leq \frac{\pi}{3}, \tag{33}$$

in terms of the reduced wave number $\hat{k}$, around the K′ and K points, respectively. The boundary point $ak = -\pi$ of the K′ point is simultaneously the boundary point $ak = \pi$ of the K point in another Brillian zone, as illustrated in Fig.13: They are physically the same point and to be identified.

4.3 Dirac electrons in triangular Graphene

Our main purpose is to apply the above result to the analysis of the zero-energy sector of the trigonal zigzag nanodisk [Fig.12]. The envelope function of the trigonal zigzag nanodisk can be constructed by making a linear combination of envelope functions for three trigonal corners. We consider the trigonal region whose corners are located at $z_1 = (L, 0), z_2 = (-L, 0)$, $z_3 = \left(0, \sqrt{3}L\right)$. As the boundary conditions we impose $\phi(z_1) = \phi(z_2) = \phi(z_3) = 0$. The resultant envelope function is obtained around the K point ($\hat{k} > 0$) as

$$\phi(z) = e^{i\hat{k}z} - e^{i\hat{k}L}e^{i\hat{k}(z-L)\exp[-2\pi i/3]} - e^{-i\hat{k}L}e^{i\hat{k}(z+L)\exp[2\pi i/3]} \tag{34}$$

up to a normalization constant. The envelope function around the K′ point ($\hat{k} < 0$) is given by $\phi(z^*)$. We display the density of the wave function $|\phi(z)|^2$ in Fig.12.

The wave number is quantized for a finite edge such as in the trigonal nanodisk. We can determine it as follows. We focus on the wave function $\psi_{\mathrm{A}}^{\tau}(\boldsymbol{x})$ at one of the A sites on an edge. There are N links along one edge of the size-N trigonal nanodisk. We can show that the correction terms are exactly cancelled out for these N links, and we obtain precisely $\Theta^{\tau}(a/2, N) = Nak$. On the other hand, the phase shift is π at the corner. The total phase shift is $3Nak + 3\pi$, when we encircle the nanodisk once. For the single-valueness of the wave function it is necessary that $3Nak + 3\pi = 2n\pi$, or

$$\hat{k}_n = \pm\frac{(2n+1)\,\pi}{3Na}, \qquad 0 \leq n \leq \frac{N-1}{2}, \tag{35}$$

with an integer n. The allowed region of the wave number is given by (32). The wave number is quantized as

$$k_n = \pm\left[\frac{2n+1}{3N} + \frac{2}{3}\right]\frac{\pi}{a}, \qquad 0 \leq n \leq \frac{N-1}{2}. \tag{36}$$

When N is even, there are $N/2$ states for $k_n > 0$ and $N/2$ states for $k_n < 0$. When N is odd, there are $(N-1)/2$ states for $k_n > 0$ and $(N-1)/2$ states for $k_n < 0$. Additionally, there seem

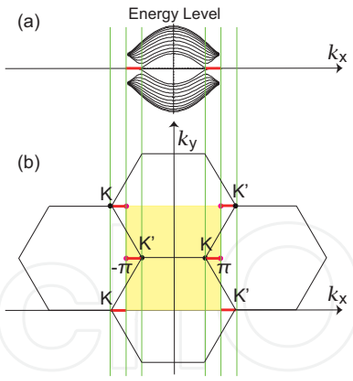

Fig. 13. (a) The energy spectrum in an infinitely long graphene edge. The flat band appears in the region indicated in red. (b) We take the Brillouin zone as indicated in yellow. The flat band appears in the region indicated in red. The boundary points at $\pm\pi$ are identified.

to appear two states with $k_n = \pm\pi/a$ at $n = (N-1)/2$. However, they are identified with one another, since they are located at the boundary of the Brillouin zone [13].
As we have reviewed in Section 3.4, the symmetry group of the trigonal nanodisk is C_{3v}, whose properties are summarized in the table (6). The mirror symmetry is equivalent to the exchange of the K and K' points. With respect to the rotation there are three elements $\mathfrak{c}_3^0$, $\mathfrak{c}_3$, $\mathfrak{c}_3^2$, which correspond to 1, $e^{2\pi i/3}$, $e^{4\pi i/3}$. Accordingly, the phase shift of one edge is 0, $2\pi/3$, $4\pi/3$. They are determined by the conditions

$$Nak_n + \pi = 2n\pi, \quad Nak_n + \pi = 2n\pi + \frac{2\pi}{3}, \quad Nak_n + \pi = 2n\pi + \frac{4\pi}{3}, \tag{37a}$$

with an integer n, respectively. It follows that the state, indexed by the edge momentum k_n as in (36), are grouped according to the representation of the trigonal symmetry group C_{3v} as follows,

$$\left.\begin{array}{l} A_1 \text{ (singlet)} : |k_n^0\rangle + |-k_n^0\rangle, \\ A_2 \text{ (singlet)} : |k_n^0\rangle - |-k_n^0\rangle, \end{array}\right\} \; k_n^0 = \frac{6n+3}{3Na}\pi, \\ E \text{ (doublet)} : |k_n^\pm\rangle, \quad |-k_n^\pm\rangle, \;\; k_n^\pm = \frac{6n\pm 1}{3Na}\pi, \tag{38}$$

where the momentum k_n^α is subject to the condition (32). It follows that

$$\left\lfloor \frac{N+1}{3} \right\rfloor \le n \le \left\lfloor \frac{N}{2} \right\rfloor, \tag{39}$$

where $\lfloor a \rfloor$ denotes the maximum integer equal to or smaller than a, and $\lceil a \rceil$ denotes the minimum integer equal to or larger than a. The numbers of doublets (E-mode) and singlets (A_1-mode or A_2-mode) are given by

$$\left\lfloor \frac{N+1}{3} \right\rfloor, \quad N - 2\left\lfloor \frac{N+1}{3} \right\rfloor, \tag{40}$$

respectively.

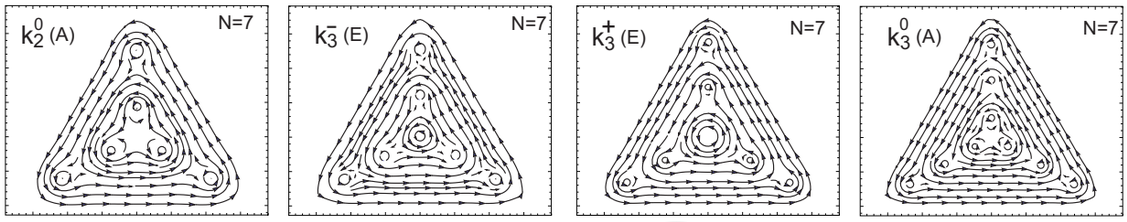

Fig. 14. Probability density flow for the state $|k_n^{(0,\pm)}\rangle$ in the nanodisk with $N = 7$. The representation is indicated in the parenthesis. A vortex appears at the center of mass for the state belonging to the E (doublet) representation. It is interesting that the winding number is 2 in the state $|k_n^+\rangle$. A circulating current along the closed edge confines flux and generates a vortex texture respecting the trigonal symmetry.

4.3.1 Probability density flow (Berry connection)

To see the meaning of the wave number k_n^α more in detail, we have calculated the probability density flow

$$\mathcal{A}_i(x,y) = -i\phi^*(x,y)\partial_i\phi(x,y) \tag{41}$$

for various states, which we show for the case of $N = 7$ in Fig.14. We observe clearly a texture of vortices: The number of vortices are $6, 7, 7, 9$ for $|k_2^0\rangle$, $|k_3^-\rangle$, $|k_3^+\rangle$, $|k_3^0\rangle$, respectively. The vortex at the center of mass must have the winding number 2 in $|k_3^+\rangle$. In general, the total winding number $N_{\rm vortex}$ is calculated by

$$N_{\rm vortex} = \frac{-i}{2\pi}\oint dx_i \,\frac{\phi^*(x,y)\partial_i\phi(x,y)}{|\phi(x,y)|^2} = N + m - 1, \tag{42}$$

with $m = 0, 1, 2, \cdots, \lfloor (N-1)/2 \rfloor$ in the size-N nanodisk, where the integration is made along the closed edge of a nanodisk. $N_{\rm vortex} = 3n$ for k_n^0, $N_{\rm vortex} = 3n+1$ for k_{n+1}^- and $N_{\rm vortex} = 3n+2$ for k_n^+. The wave functions are classified in terms of modulo of the total winding number: the wave function belongs to the E-representation and has chiral edge mode for $N_{\rm vortex} \equiv 1, 2 \pmod 3$, and belongs to the A-representation and has non-chiral edge mode for $N_{\rm vortex} \equiv 0 \pmod 3$. There are n vortices along the y-axis in the state $|k_n^\alpha\rangle$. The state $|k_n^\pm\rangle$, being the E-mode, has a vortex at the center of mass, where the winding number is 2 in the state $|k_n^+\rangle$. On the other hand, the state $|k_n^0\rangle$ does not have a vortex at the center of mass, and the combinations $|k_n^0\rangle \pm |-k_n^0\rangle$ belong to the A_1 and A_2 representations, respectively.

To demonstrate the above statement, we search for zero points of the wave function, where vortices appear. The probability density along the y-axis is given by

$$|\psi(y)|^2 = \left(-e^{-ky} + 2e^{k\left(y-\sqrt{3}Na/2\right)/2}\cos\frac{\sqrt{3}k\left(y+\sqrt{3}Na/2\right)}{2}\right)^2, \tag{43}$$

which is found to have n zeros for $k = k_n^{(\pm)}$. In particular we examine the emergence of a vortex at the center of mass, where we may expand $\psi(z)$ as

$$\psi(z) = C_0 + C_1 k\left(z - i\frac{Na}{2\sqrt{3}}\right) + C_2 k^2\left(z - i\frac{Na}{2\sqrt{3}}\right)^2 + \cdots. \tag{44}$$

The coefficient C_0 vanishes at

$$k = \frac{6n \pm 1}{3Na}\pi, \tag{45}$$

namely, for the state $|k_n^{\pm}\rangle$. Furthermore, C_1 vanishes at

$$k = \frac{6n+1}{3Na}\pi. \tag{46}$$

Hence we confirm that a vortex with the winding number 2 appears in the state $|k_n^{+}\rangle$. We can check that C_2 does not vanish where C_0 vanishes. Namely, there are no vortices with the winding number 3.
These vortices are present inside the nanodisk where the electron density is almost zero. The situation is similar to a flux confined within a solenoid or within a superconducting ring, where no electrons are present in the domain where the magnetic flux exists. The electric current confining the flux generates the Aharonov-Bohm phase (42) associated with vortices. Vortices make a texture respecting the trigonal symmetry C_{3v} within a nanodisk.

4.3.2 Magnetic vortices

Charged particles propagating along a closed edge generates magnetic field. The electromagnetic interaction is described in terms of the electromagnetic potential $\boldsymbol{A}$, which is introduced to the system by way of the Peierls substitution $\partial_j \to \partial_j + ieA_j/\hbar$. Here we consider the lowest order approximation, where $\phi_{\rm A}^{\rm K}(\boldsymbol{x})$ is not modified from (34) in the presence of the electromagnetic interaction. Then, from the Weyl equation (28), we derive

$$eA_i(\boldsymbol{x}) = -i\hbar\frac{\phi_{\rm A}^{\rm K*}(\boldsymbol{x})\partial_i\phi_{\rm A}^{\rm K}(\boldsymbol{x})}{|\phi_{\rm A}^{\rm K}(\boldsymbol{x})|^2} = \hbar\frac{\mathcal{A}_i(\boldsymbol{x})}{|\phi_{\rm A}^{\rm K}(\boldsymbol{x})|^2}. \tag{47}$$

The potential $A_i(\boldsymbol{x})$ exhibits the same texture of vortices as in Fig.14. The magnetic field is given by

$$B(x,y) = \nabla \times A(\boldsymbol{x}) = \frac{2\pi\hbar}{e}\sum_n \nu_n \delta\left(z - z_n\right), \tag{48}$$

where ν_n stands for winding number of the vortex at $z = z_n$. Hence a texture of vortices in the Berry connection leads to a texture of magnetic vortices. This δ-function type magnetic field would be smoothed out in a rigorous analysis of the coupled system of the Maxwell equation and the Weyl equation.
We have shown that the winding number of the vortex at the center of the nanodisk is $0, 1, 2$ in the state $|k_n^0\rangle, |k_n^-\rangle, |k_n^+\rangle$, respectively. By tuning the chemical potential any of them is made the ground state. As far as we are aware of, the vortex with the winding number 2 has never been found in all branches of physics. This is because two vortices with the winding number 1 have lower energy than one vortex with the winding number 2 in general. In the present case the disintegration of a vortex into two is prohibited by the trigonal symmetry.
As is well known, a single flux quantum has experimentally been observed in superconductor by using an electron-holographic interferometry(70). Then, in principle it is possible to observe a vortex texture in nanodisk as well. Furthermore, by attaching a superconductor film one may observe a disintegration of a vortex into two when the flux enters into the superconductor from the nanodisk. This would verify the winding number 2 of a vortex.

5. Electron-electron interactions

In this section we make an investigation of electron-electron interaction effects in the zero-energy sector. The spin stiffness is quite large due to large exchange interactions,

which means that a nanodisk is a rigid ferromagnet. The system is well described by the infinite-range Heisenberg model, which is exactly solvable. Constructing the partition function, we explore thermodynamical properties(47; 65). A sharp peak emerges at a certain temperature in the specific heat, which we interpret as a quasi-phase transition between quasiferromagnetic and paramagnetic states.

5.1 Exchange interactions

Let us include the Coulomb interaction between electrons in the zero-energy sector. We take two states $|f_\alpha\rangle$ and $|f_\beta\rangle$, $\alpha \neq \beta$, each of which can accommodate two electrons with up and down spins at most. The two-state system is decomposed into the spin singlet $\chi_{\rm S}$ and the spin triplet $\chi_{\rm T}$ with the normalized wave functions,

$$f^{\rm SS}_{\alpha\beta}(\boldsymbol{x},\boldsymbol{x}') = \frac{1}{\sqrt{2}}\Big(f_\alpha(\boldsymbol{x})f_\beta(\boldsymbol{x}') + f_\alpha(\boldsymbol{x}')f_\beta(\boldsymbol{x})\Big)\,\chi_{\rm S}, \tag{49a}$$

$$f^{\rm ST}_{\alpha\beta}(\boldsymbol{x},\boldsymbol{x}') = \frac{1}{\sqrt{2}}\Big(f_\alpha(\boldsymbol{x})f_\beta(\boldsymbol{x}') - f_\alpha(\boldsymbol{x}')f_\beta(\boldsymbol{x})\Big)\,\chi_{\rm T}. \tag{49b}$$

The Coulomb energies are summarized as

$$\langle f^{\rm SS}_{\alpha\beta}|H_{\rm C}|f^{\rm SS}_{\alpha\beta}\rangle = U_{\alpha\beta} + J_{\alpha\beta}, \qquad \langle f^{\rm ST}_{\alpha\beta}|H_{\rm C}|f^{\rm ST}_{\alpha\beta}\rangle = U_{\alpha\beta} - J_{\alpha\beta}, \tag{50}$$

where $U_{\alpha\beta}$ and $J_{\alpha\beta}$ are the direct and exchange energies. In the many-state system the effective Hamiltonian is derived as

$$H_{\rm D} = \sum_{\alpha\geq\beta} U_{\alpha\beta} n(\alpha)\, n(\beta) - \frac{1}{2}\sum_{\alpha>\beta} J_{\alpha\beta}[4\boldsymbol{S}(\alpha)\cdot\boldsymbol{S}(\beta) + n(\alpha)\, n(\beta)], \tag{51}$$

where $n(\alpha) = d^\dagger_\sigma(\alpha)d_\sigma(\alpha)$ is the number operator and $\boldsymbol{S}(\alpha) = \frac{1}{2}d^\dagger_\sigma(\alpha)\boldsymbol{\tau}_{\sigma\sigma'}d_{\sigma'}(\alpha)$ is the spin operator, with $d_\sigma(\alpha)$ the annihilation operator of electron with spin $\sigma = \uparrow,\downarrow$ in the zero-energy state $|f_\alpha\rangle$: $\boldsymbol{\tau}$ is the Pauli matrix. Note the existence of the on-state Coulomb term $U_{\alpha\alpha}n(\alpha)\, n(\alpha)$ in the effective Hamiltonian (51).

We expand $U_{\alpha\beta}$ and $J_{\alpha\beta}$ in terms of the Wannier functions with the use of (5),

$$U_{\alpha\beta} = \sum_s \omega^\alpha_i\omega^\alpha_j\omega^\beta_k\omega^\beta_l \int d^3x d^3y\ \varphi^*_i(\boldsymbol{x})\varphi_j(\boldsymbol{x})V(\boldsymbol{x}-\boldsymbol{y})\varphi^*_k(\boldsymbol{y})\varphi_l(\boldsymbol{y}), \tag{52a}$$

$$J_{\alpha\beta} = \sum_s \omega^\alpha_i\omega^\alpha_j\omega^\beta_k\omega^\beta_l \int d^3x d^3y\ \varphi^*_i(\boldsymbol{x})\varphi_j(\boldsymbol{y})V(\boldsymbol{x}-\boldsymbol{y})\varphi^*_k(\boldsymbol{y})\varphi_l(\boldsymbol{x}). \tag{52b}$$

The dominant contributions come from the on-site Coulomb terms with $i=j=k=l$ both for the direct and exchange energies. We thus obtain

$$U_{\alpha\beta} \simeq J_{\alpha\beta} \simeq U\sum_i (\omega^\alpha_i\omega^\beta_i)^2, \tag{53}$$

with

$$U \equiv \frac{e^2}{4\pi\varepsilon}\int d^3x d^3y\ \varphi^*_i(\boldsymbol{x})\varphi_i(\boldsymbol{x})\frac{1}{|\boldsymbol{x}-\boldsymbol{y}|}\varphi^*_i(\boldsymbol{y})\varphi_i(\boldsymbol{y}). \tag{54}$$

The Coulomb energy U is of the order of 1eV because the lattice spacing of the carbon atoms is $\sim$ 1Å in graphene. The nearest neighbor Coulomb interaction vanishes since no electrons exist in B sites: See Fig.6. It is straightforward to take into account higher order corrections but the effects are only to enhance the ferromagnetic order. The essential properties of the Coulomb interactions are well described only by taking the on-site terms.

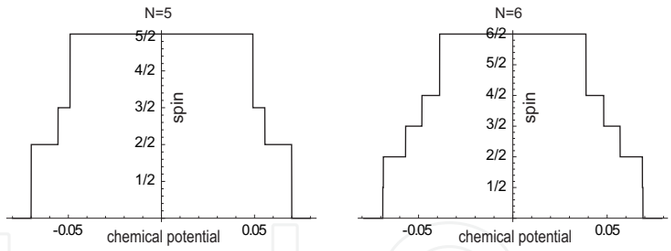

Fig. 15. The nanodisk spin as a function of the chemical potential. The vertical axis is the spin, where the highest value is $N/2$. The horizontal axis is the chemical potential μ. The nanodisk spin is controlled by changing μ.

5.2 Zero-energy splitting due to coulomb interactions

We have shown that the N-fold degeneracy in the zero-energy sector is resolved by Coulomb interactions. The Coulomb Hamiltonian has the trigonal symmetry C_{3v}, and the energy spectrum splits into different levels according to its representation. The energy split is approximately scaled by $U_{\alpha\alpha}$.

There exists additionally the spin-degeneracy in the noninteracting Hamiltonian: The total degeneracy is $2N$. The spin degeneracy is broken spontaneously with the introduction of Coulomb interactions. The splitting is symmetric with respect to the zero-energy level. At half-filling, electrons with the identical spin fill all energy levels under the Fermi energy. Then, the spin of the ground state is $N/2$, and it is a ferromagnet. We show the energy spectrum for $N = 5, 6$ in Fig.15.

It is interesting that we can control the total spin by changing the chemical potential μ. Let us assume that all spins are up polarized in the ground state. As μ increases from zero and reaches the next energy level, down-spin electrons fill the level. As a result, the ground-state spin is reduced by $1/2$ or 1 when the energy level is singlet or doublet, respectively. When μ increases higher than the highest energy level, the total spin becomes 0 and the ferromagnet disappears. The same results apply to the case when μ decreases. We show the total spin as a function of the chemical potential μ in Fig.15.

In our analysis the interaction effects are treated only within the subspace of zero-energy states. It is desirable to derive an effective low-energy Hamiltonian by integrating out the higher excitation levels in a renormalization procedure rather than just neglecting these levels. This has actually been done by functional-renormalization-group analysis recently(71). Our treatment neglecting the renormalizations by the higher levels are shown to be valid by functional-renormalization-group analysis. Furthermore, first-principle calculations of electronic structure of graphene nanodisk have been carried out, which are found to be consistent with our results(37; 38; 42). Result are shown in Fig.16.

5.3 SU(N) Approximation

As we have shown numerically, all $J_{\alpha\beta}$ are of the same order of magnitude for any pair of α and β, implying that the SU(N) symmetry is broken but not so strongly in the Hamiltonian (51). It is a good approximation to start with the exact SU(N) symmetry, where we set $J_{\alpha\beta} = U_{\alpha\beta} = J$. (We set the average of $J_{\alpha\beta}$ as J in the size-N nanodisk.) Then, the zero-energy sector is described by the Hamiltonian $H_{\rm D} = H_{\rm S} + H_{\rm U}$, with

$$H_{\rm S} = -J \sum_{\alpha \neq \beta} \boldsymbol{S}(\alpha) \cdot \boldsymbol{S}(\beta), \qquad H_{\rm U} = \frac{J}{4} \sum_{\alpha \neq \beta} n(\alpha)\, n(\beta) + J \sum_{\alpha} n(\alpha). \tag{55}$$

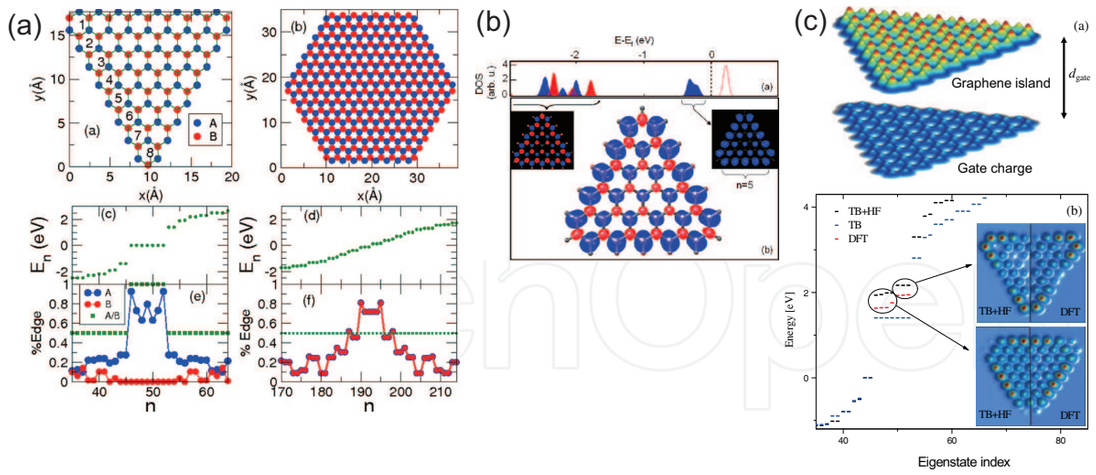

Fig. 16. The first-principle calculation of graphene nanodisdks. Fig. (a) is taken from the work of Fernández-Rossier et. al (37), Fig. (b) is taken from the work of Wang et. al (38) and Fig. (c) is taken form the work of Güçlü et al.(42).

The term H_{S} is known as the infinite-range Heisenberg model. We rewrite them as

$$H_{\mathrm{S}} = -J\boldsymbol{S}_{\mathrm{tot}}^2 + \frac{3}{4}Jn_{\mathrm{tot}}, \qquad H_{\mathrm{U}} = \frac{J}{4}(n_{\mathrm{tot}}^2 + 1), \tag{56}$$

where $n_{\mathrm{tot}} = \sum_{\alpha} n(\alpha)$ is the total electron number.
The ground states of nanodisks are half filled. We restrict the Hilbert space to the half-filling sector, where $n(\alpha) = n_{\uparrow}(\alpha) + n_{\downarrow}(\alpha) = 1$. The Hamiltonian (56) is reduced to the Heisenberg model,

$$H_{\mathrm{S}} = -J\boldsymbol{S}_{\mathrm{tot}} \cdot \boldsymbol{S}_{\mathrm{tot}}, \tag{57}$$

where we have neglected an irrelevant constant term, $(3/4)JN$. This is exactly diagonalizable, $H_{\mathrm{S}}|\Psi\rangle = E_s|\Psi\rangle$, with $E_s = -Js(s+1)$, where s takes values from $N/2$ down to $1/2$ or 0, depending on whether N is odd or even, $s = \frac{N}{2}, \frac{N}{2}-1, \frac{N}{2}-2, \cdots, \quad s \geq 0$. The Hilbert space is diagonalized, $\mathbb{H} = \otimes^N \mathbb{H}_{1/2} = \oplus^{g_N(s)}\mathbb{H}_s$, where $\mathcal{H}_s$ denotes the $(2s+1)$ dimensional Hilbert space associate with an irreducible representation of SU(2). The multiplicities $g_N(s)$ satisfies the recursion relation coming from the spin synthesizing rule, $g_N(s) = g_{N-1}(s-\frac{1}{2}) + g_{N-1}(s+\frac{1}{2})$. We solve this as $g_N(\frac{1}{2}N - q) = {}_N C_q - {}_N C_{q-1}$. The total degeneracy of the energy level E_s is $(2s+1)\,g_N(s)$. At half filling, the eigenstate of the Hamiltonian H_{D} is labeled as $|\Psi\rangle = |n_{\mathrm{tot}}, s, m\rangle$, where s is the total spin and m is its z-component.

5.4 Thermodynamical properties

We have a complete set of the eigenenergies together with their degeneracies. The partition function of the nanodisk with size N is exactly calculable(47). According to the standard procedure we can evaluate the specific heat $C(T)$, the entropy $S(T)$, the magnetization $\langle \boldsymbol{S}_{\mathrm{tot}}^2 \rangle$ and the susceptibility $\chi = \left(\langle S_{z,\mathrm{tot}}^2 \rangle - \langle S_{z,\mathrm{tot}} \rangle^2 \right) / (k_{\mathrm{B}}T)$from this partition function. The ground-state value of the total spin is $S_g = \sqrt{(N/2)(N/2+1)}$. The entropy is given by $S(0) = k_{\mathrm{B}} \log(N+1)$ at zero temperature. We display them in Fig.17 for size $N = 1, 2, 2^2, \cdots 2^{10}$.
There appear singularities in thermodynamical quantities as $N \to \infty$, which represent a phase transition at T_c between the ferromagnet and paramagnet states, $T_c = JN/(2k_{\mathrm{B}})$. For finite

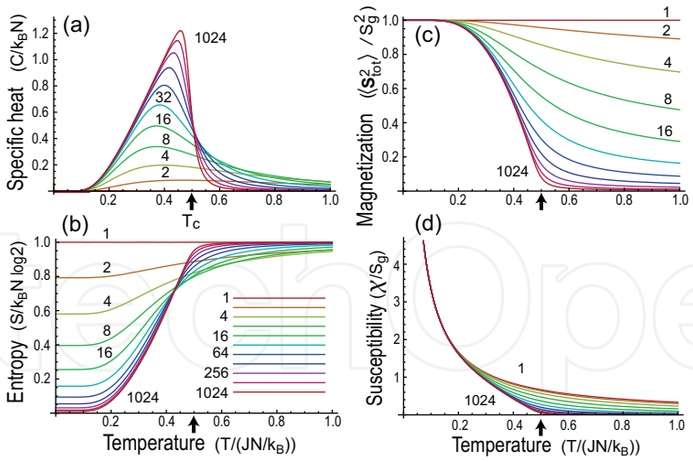

Fig. 17. Thermodynamical properties of the nanodisk-spin system. (a) The specific heat C in unit of $k_{\rm B}N$. (b) The entropy S in unit of $k_{\rm B}N\log 2$. (c) The magnetization $\left\langle \boldsymbol{S}_{\rm tot}^2 \right\rangle$ in unit of S_g^2. (d) The susceptibility χ in unit of S_g. The size is $N = 1, 2, 2^2, \cdots 2^{10}$. The horizontal axis stands for the temperature T in unit of $JN/k_{\rm B}$. The arrow represents the phase transition point T_c in the limit $N \to \infty$.

N, there are steep changes around T_c, though they are not singularities. It is not a phase transition. However, it would be reasonable to call it a quasi-phase transition between the quasiferromagnet and paramagnet states. Such a quasi-phase transition is manifest even in finite systems with $N = 100 \sim 1000$.

The specific heat and the magnetization take nonzero-values for $T > T_c$ [Fig.17(a),(c)], which is zero in the limit $N \to \infty$. The entropy for $T > T_c$ is lower than that of the paramagnet [Fig.17(b)]. These results indicate the existence of some correlations in the paramagnet state.

As shown in Fig.17(d), the susceptibility χ always shows the Curie-Weiss low $\chi \propto 1/T$ near $T = 0$, and exhibits also a behavior showing a quasi-phase transition at $T = T_c$. In the finite system, the expectation value of $S_{z,\rm tot}$ is always zero because there is no spontaneous symmetry breakdown in the finite system, and the behavior is that of paramagnet.

5.5 Lieb's theorem

We make some remarkable observations on the spin of a nanodisk. Due to the exchange interaction in the Hamiltonian (51), all spins are spontaneously polarized into a single direction. Since the exchange energy is as large as the direct energy, which is the order of a few hundred meV, the spin stiffness $J_{\alpha\beta}$ is quite large, implying that nanodisks are almost rigid ferromagnets. We refer to the total spin of a nanodisk, $\boldsymbol{S}_{\rm tot} = \sum_\alpha \boldsymbol{S}(\alpha)$, as the nanodisk spin. The size-N nanodisk spin is $\frac{1}{2}N$ in the ground state.

This is consistent with Lieb's theorem(72) valid for the Hubbard model. As far as only the on-site Coulomb interactions are taken into account, the electron-electron interaction is approximated by the Hubbard model,

$$H_U = U \sum_i d_{i\uparrow}^\dagger d_{i\uparrow} d_{i\downarrow}^\dagger d_{i\downarrow}, \tag{58}$$

where U is given by (54): It is estimated(73) that $U \approx t$. Lieb's theorem states that, in the case of repulsive electron-electron interactions ($U > 0$), a bipartite system at half-filling has the ground state whose total spin is $S_{\rm tot} = \frac{1}{2}|N_A - N_B|$, where N_A and N_B are the numbers of

sites in sublattices A and B, respectively [Fig.6]. They are given by (**??**), and hence $S_{\rm tot} = \frac{1}{2}N$ for the size-N nanodisk.

6. Large size triangular graphene

In this appendix we argue that our analysis based on the zero-energy sector is essentially correct, even if the size N of the nanodisk is large and the band gap becomes very narrow. In this case, the DOS of the nanodisk is decomposed into the DOS due to the edge, which is δ-function like, and the DOS due to the bulk, which is almost continuous. The correction to the magnetization from the bulk part is shown to be of the order of $1/N$ with respect to the one from the edge part in the zero-temperature limit.

6.1 Density of states

It is possible to derive an analytical expression for the density of states of graphene per unit cell(74), which has the form

$$\rho\left(\varepsilon\right) = \frac{4}{\pi^2}\frac{|\varepsilon|}{t^2}\frac{1}{\sqrt{Z_0}}K\left(\sqrt{\frac{Z_1}{Z_0}}\right), \tag{59}$$

with

$$Z_0 = \left\{ \begin{array}{cc} \left(1+\left|\frac{\varepsilon}{t}\right|\right)^2 - \left((\varepsilon/t)^2-1\right)^2/4; & -t \le \varepsilon \le t \\ 4\left|\varepsilon/t\right|; & -3t \le \varepsilon \le -t \vee t \le \varepsilon \le 3t \end{array} \right|, \tag{60a}$$

$$Z_1 = \left\{ \begin{array}{cc} 4\left|\varepsilon/t\right|; & -t \le \varepsilon \le t \\ \left(1+\left|\frac{\varepsilon}{t}\right|\right)^2 - \left((\varepsilon/t)^2-1\right)^2/4; & -3t \le \varepsilon \le -t \vee t \le \varepsilon \le 3t \end{array} \right|, \tag{60b}$$

where $K\left(x\right)$ is the complete elliptic integral of the first kind. Thus, near the Dirac point we find

$$\rho\left(\varepsilon\right) = \frac{2A_c}{\pi v_{\rm F}^2}\left|\varepsilon\right|, \tag{61}$$

where A_c is the unit cell area, $A_c = 3\sqrt{3}a^2/2$.

For large N nanodisks, the band gap decreases inversely proportional to the size. One may wonder if our analysis based on only the zero-energy sector is relevant. Indeed, the size of experimentally available nanodisks is as large as $N = 100 \sim 1000$. We would like to argue that our analysis of the zigzag trigonal nanodisk captures the basic nature of nanodisks even for such a large size system.

It is important to remark that each energy level is at most two-fold degenerate except for the states at $\varepsilon = 0$ and $\varepsilon = t$ irrespective to its size N, as illustrated in Fig.18. The degeneracy is governed by the representation (6) of the trigonal symmetry group C_{3v}. Hence, in the limit $N \to \infty$, the density of state (DOS) of the zigzag trigonal nanodisk reflects the following two aspects; one is that there appear van-Hove singularities at $\varepsilon = 0$ and $\varepsilon = t$. The other is that the DOS shows a continuous and dense structure, which has the same structure of the bulk graphene [Fig.18] except for the contributions from these singularities. Namely, near the Fermi energy, the DOS consists of that of the bulk graphene and an additional peak at the zero-energy states due to the edge states for $N \gg 1$, as illustrated in Fig.18. Hence, together with spin degrees of freedom, it behaves as

$$D\left(\varepsilon\right) = 2cN_c\left|\varepsilon\right| + 2N\delta\left(\varepsilon\right), \tag{62}$$

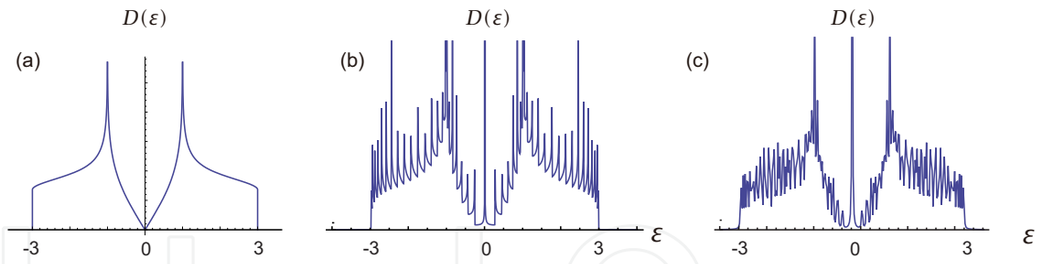

Fig. 18. The density of state of a (a) graphene, (b) graphene nanoribbon and (c) graphene nanodisk. The horizontal axis is the energy ε.

with $c = 2A_c/\pi v_{\mathrm{F}}^2$. The linear term is due to the bulk states as given by (61), and the Dirac delta function term is due to the edge states. The important point is that the edge-state peak is clearly distinguished from the DOS due to the bulk part. It is enough to take into account only the zero-energy sector to analyze physics near the Fermi energy, since the contribution from the edge states is dominant.

6.2 Magnetism

For definiteness we explicitly calculate the magnetization of a nanodisk when its size is large. We start with the Hubbard Hamiltonian,

$$H = \sum_{ij\sigma} t_{ij} c_{i\sigma}^{\dagger} c_{i\sigma} + U \sum_{i} c_{i\uparrow}^{\dagger} c_{i\uparrow} c_{i\downarrow}^{\dagger} c_{i\downarrow} = \sum_{k\sigma} \varepsilon(k)\, c_{k\sigma}^{\dagger} c_{k\sigma} + U \sum_{kk'q} c_{k+q\uparrow}^{\dagger} c_{k'-q\downarrow}^{\dagger} c_{k'\downarrow} c_{k\uparrow}. \tag{63}$$

In the Hartree-Fock approximation the Hamiltonian is transformed into

$$H_{MF} = \sum \left(\varepsilon_k + \frac{U}{2N_{\mathrm{C}}} \langle n \rangle + \sigma \Delta \right) c_{k\sigma}^{\dagger} c_{k\sigma} - N_{\mathrm{C}} U \langle n_{\uparrow} \rangle \langle n_{\downarrow} \rangle ,$$

where $N_{\mathrm{C}} = N^2 + 6N + 6$,

$$\Delta = \frac{U}{2N_{\mathrm{C}}} \langle m \rangle + \frac{h}{2}, \tag{64}$$

with the external magnetic field h and $\langle n_{\sigma} \rangle = \frac{1}{2} (\langle n \rangle + \sigma \langle m \rangle)$, or $\langle n \rangle = \langle n_{\uparrow} \rangle + \langle n_{\downarrow} \rangle$, $\langle m \rangle = \langle n_{\uparrow} \rangle - \langle n_{\downarrow} \rangle$. The statistical mean values $\langle n \rangle$ and $\langle m \rangle$ are determined self-consistently as

$$\langle n \rangle = \int d\varepsilon \rho(\varepsilon) \left[f(\varepsilon - \Delta) + f(\varepsilon + \Delta) \right], \tag{65}$$

$$\langle m \rangle = \int d\varepsilon \rho(\varepsilon) \left[f(\varepsilon - \Delta) - f(\varepsilon + \Delta) \right], \tag{66}$$

with the Fermi distribution function $f(x) = 1/(\exp[(x-\mu)/k_{\mathrm{B}}T] + 1)$. We can rewrite (66) into

$$\langle m \rangle = \int d\varepsilon \rho(\varepsilon) \left[\tanh \frac{\beta(\varepsilon + \Delta)}{2} - \tanh \frac{\beta(\varepsilon - \Delta)}{2} \right]. \tag{67}$$

Substituting the formula (62) of the DOS into the Storner equation (66), we obtain

$$\langle m \rangle = N \tanh \frac{\beta \Delta}{2} + c N_{\mathrm{c}} \left[\Delta^2 + \frac{1}{\beta^2} \left\{ \frac{\pi^2}{3} + 4 \mathrm{Li}_2 \left(-e^{-\beta \Delta} \right) \right\} \right], \tag{68}$$

with the dilogarithm function $\mathrm{Li}_2(x)$. It is difficult to solve this equation for $\langle m \rangle$ self-consistently at general temperature T. We examine two limits, $T \to 0$ and $T \to \infty$.

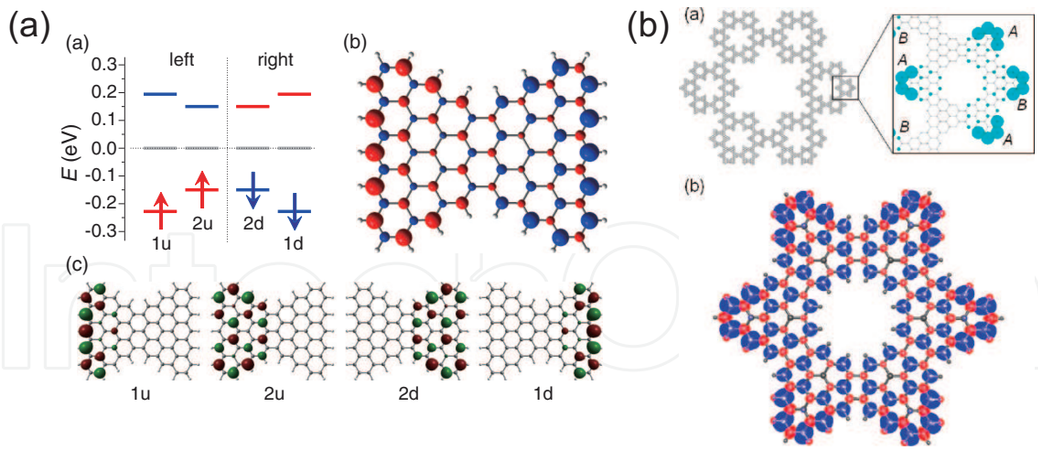

Fig. 19. (a) Clar goblet or bow-tie shaped graphene nanodisk. (b) Fractal sturucture of star of David graphene nanodisk. Fig (a) is taken from the work of Wang et. al (39), and Fig. (b) is taken from the work of Wang et al (38).

For the zero temperature ($T \to 0$) we obtain

$$\langle m \rangle = N + c\frac{U^2}{4N_C} \langle m \rangle^2 + \frac{cUh}{2} \langle m \rangle + O(h^2). \tag{69}$$

The magnetization $\langle m \rangle$ is determined by solving (69). Because $|\langle m \rangle| \leq N$, it follows that $\langle m \rangle = N + O(1)$. The contribution from the bulk gives a negligible correction to the total magnetization. Hence the magnetization is $\langle m \rangle = N$, and the ground state is fully poralized whenever $U \neq 0$. Ferromagnetism occurs irrespective of the strength of the Coulomb interaction.
The magnetization is propotional not to N_c but N. In this sence the ground state of nanodisk is not bulk ferromagnet but surface ferromagnet, which is consistent with the previous result. We next investigate the high temperatuer limit ($T \to \infty$). Using the Taylor expansion of the dilogarithm function,

$$\mathrm{Li}_2\left(-e^{-\beta\Delta}\right) = -\frac{\pi^2}{12} + \beta\Delta \log 2 - \frac{\beta^2\Delta^2}{4} + \frac{\beta^3\Delta^3}{24} + \cdots, \tag{70}$$

we find

$$\langle m \rangle = N \tanh \frac{\beta\Delta}{2} + cN_c \left[\frac{4\Delta}{\beta} \log 2 + \frac{\beta\Delta^3}{6} + \cdots \right]. \tag{71}$$

The leading term is the second term, and hence the main contribution comes from the bulk. The solution is only $\langle m \rangle = 0$ for which $\Delta = 0$. There is no magnetization at high temperature.

7. Complex structure of nanodisk

7.1 Bowtie-shaped graphene nanodisk

A bowtie-shaped graphene nanodisk is proposed by Wang et. al(39). A bowties-shaped graphene nanodisk is composed of two trigonal graphene nanodisks sharing one hexagon: See Fig.19. Lieb's theorem predicts the ground state with $S = 0$. On the other hand, there are degenerate zero-energy states predicted from the graph theory(68). To satisfy the spin-singlet ground state, the ground electronic configuration exhibits antiferromagnetic ordering.

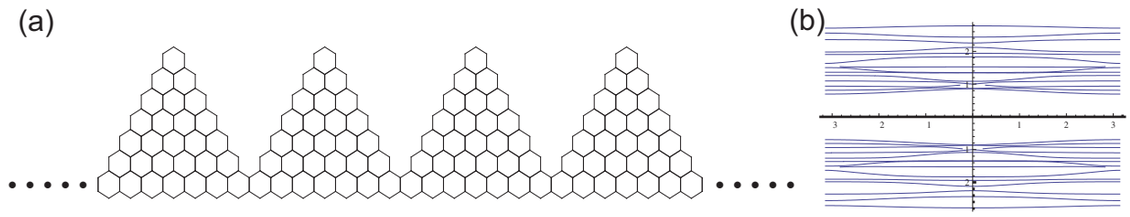

Fig. 20. (a) Illustration of nanodisk array. (b) Band structure.

7.2 "Star of David" graphene nanodisk

A "Star of David" shape graphene nanodisk is proposed by Wang et. al(38). The structure is fractal and generated by repeatedly overlapping two triangles in opposite directions and removing the overlap portion: See Fig.19. The structure has a fractal dimension,

$$\frac{\log 1/6}{\log 1/3} = 1.62. \tag{72}$$

The total spin increases exponentially with the fractal level q as $S_q = S_0 2^q$, where S_0 is the spin of the initial graphene triangle(38). The increase of the total spin is due to the increase of the boundary length, a hallmark of fractal structures.

7.3 Nanodisk array

We investigate nanodisk arrays, which are materials that nanodisks are connected in one-dimention. We show an example of trigonal zigzag nanodisk array in Fig.20(a). We show the corresponding band structure in Fig.20(b). It is intriguing that there are N-fold degenerate perfect flat band in the nanodisk with size N. This fact is also confirmed by the Leib theorem. Each nanodisk has spin N/2 and make ferromagnetic coupling between two nanodisks. In the same way we can make two-dimensional nanodisk arrays.

7.4 Nanomechanical switching

We can construct a nanomechanical switching contacting two graphene trigonal corners. We assume the angle between two corners is θ. The conductance is determined by the overlap integral of pi electrons between two corners, which is given by

$$\left|\langle p_z \cos\theta + p_y \sin\theta \, | p_z \rangle\right| = \cos^2\theta. \tag{73}$$

When the two planes are parallel ($\theta = 0$), the overlap takes the maximum value and pi-electrons can go through the contact. This is the on state. When the two planes are orthogonal ($\theta = \pi/2$), the overlap takes the minimum value and pi-electrons can not go through the contact. This is the off state. The angle is changed by nanomechanically. In this sence this system acts as a nanomechanical switch. This system could detect the angle very sensitively and be useful for detect nanomechanical oscillations.

8. Spintronic devices

We anticipate graphene derivatives to be the key elements of future nanoelectronics and spintronics. First of all, graphene is common material and ecological. In graphene, spin relaxation length is as large as $2\mu m$ due to small spin-orbit interactions. Long spin relaxation length has motivated spintronics based on graphene recently. Nevertheless, there exists a key issue yet to be resolved, that is, how to generate and manipulate spin currents. Graphene

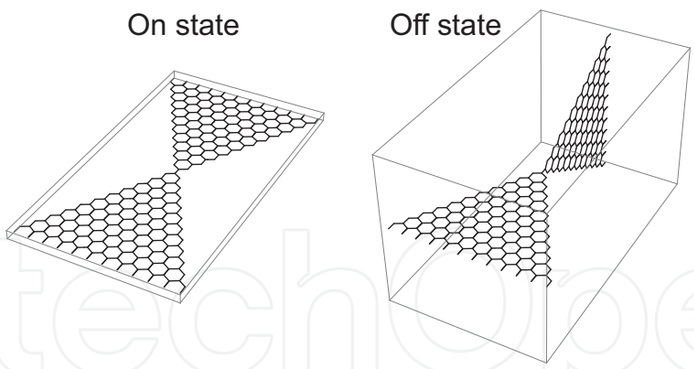

Fig. 21. Nanomechanical switching. (a) On state. (b) Off state.

nanodisks with size $N = 10 \sim 100$ would be ideal for this purpose, where localized spins are stored. In the rest of this section we shall propose a rich variety of spintronic devices made of nanodisks and leads, such as spin memory, spin valve, spin-field-effect transistor, spin diode and spin switch.

8.0.0.1 Basic properties

We summarize the relation between the spin properties of a nanodisk and an incoming electric current. First of all, being a quasiferromagnet, the nanodisk has a definite polarization. With respect to the incoming electric current there are three cases. (1) The polarized current, where all electrons have a definite polarization, rotates the nanodisk spin to that of the incoming current. (2) The unpolarized current, where the polarization of each electron is completely random, does not induce any effective magnetic field. Hence it is filtered so that the outgoing current is polarized to that of the nanodisk. (3) The partially polarized current, where the polarization of each electron is at random but the averaged polarization has a definite direction, induces a net effective magnetic field. Hence it rotates the nanodisk spin to that of the incoming current, and then is filtered so that the outgoing current is completely polarized to the averaged polarization of the incoming current. Furthermore, it is possible to control the nanodisk spin externally by applying magnetic field. Then the outgoing current has the same polarization as that of the nanodisk, irrespective of the type of incoming current. Using these properties we propose some applications of graphene nanodisks for spintronic devices.

8.0.0.2 Spin memory

The first example is a spin memory(58). For a good memory device three conditions are necessary: (i) It keeps a long life time information; (ii) Information stored in the memory can be read out without changing the information stored; (iii) It is possible to change the information arbitrarily.

First, since the life time of the nanodisk quasiferromagnet is very long compared to its size, we may use the nanodisk spin as an information. Next, we can read-out this information by applying a spin-unpolarized current. The outgoing current from a nanodisk is spin-polarized to the direction of the nanodisk spin. Thus we can obtain the information of the nanodisk spin by observing the outgoing current. Finally, the direction of the nanodisk spin can be controlled by applying a spin-polarized current into the nanodisk. Thus, the nanodisk spin satisfies the conditions as a memory device. The important point is that the size is of the order of nanometer, and it is suitable as a nanodevice.

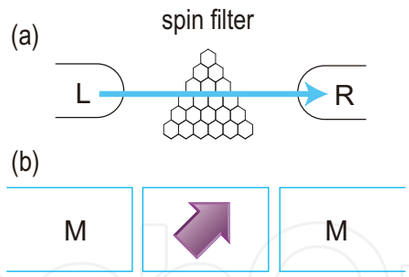

Fig. 22. (a) An electron tunnels from the left lead to the nanodisk and then to the right lead. Only electrons with the same spin direction as the nanodisk spin can pass through the nanodisk freely. As a result, when we apply a spin-unpolarized current to the nanodisk, the outgoing current is spin polarized to the direction of the nanodisk spin. Consequently, this system acts as a spin filter. (b) The system is a reminiscence of a metal-ferromagnet-metal junction.

8.0.0.3 Spin filter

We make an investigation of the spin-filter effects(64). We first analyze how spin of a nanodisk filters spin of the current by assuming that the nanodisk is a rigid ferromagnet. However, since the nanodisk is not a rigid ferromagnet but a quasiferromagnet, its spin can be controlled by the spin of the current. We analyze the reaction to the spin of the nanodisk from the spin of electrons in the current.

We go on to investigate applications of nanodisks to spintronics. The basic one is a spin filter(75). We consider a lead-nanodisk-lead system, where an electron makes a tunnelling from the left lead to the nanodisk and then to the right lead. This system is a reminiscence of a metal-ferromagnet-metal junction (Fig.22). If electrons in the lead has the same spin direction as the nanodisk spin, they can pass through the nanodisk freely. However, those with the opposite direction feel a large Coulomb barrier and are blocked (Pauli blockade)(64). As a result, when we apply a spin-unpolarized current to the nanodisk, the outgoing current is spin polarized to the direction of the nanodisk spin. Consequently, this system acts as a spin filter.

8.0.0.4 Spin valve

A nanodisk can be used as a spin valve, inducing the giant magnetoresistance effect(76–78). We set up a system composed of two nanodisks sequentially connected with leads [Fig.23]. We apply external magnetic field, and control the spin direction of the first nanodisk to be $|\theta\rangle = \cos\frac{\theta}{2}|\uparrow\rangle + \sin\frac{\theta}{2}|\downarrow\rangle$, and that of the second nanodisk to be $|0\rangle = |\uparrow\rangle$. We inject an unpolarized-spin current to the first nanodisk. The spin of the lead between the two nanodisks is polarized into the direction of $|\theta\rangle$. Subsequently the current is filtered to the up-spin one by the second nanodisk. The outgoing current from the second nanodisk is

$$I_{\uparrow}^{\text{out}} = I\cos\frac{\theta}{2}. \tag{74}$$

We can control the magnitude of the up-polarized current from 0 to I by rotating the external magnetic field. The system act as a spin valve.

8.0.0.5 Spin switch

We consider a chain of nanodisks and leads connected sequentially (Fig.22). Without external magnetic field, nanodisk spins are oriented randomly due to thermal fluctuations, and a

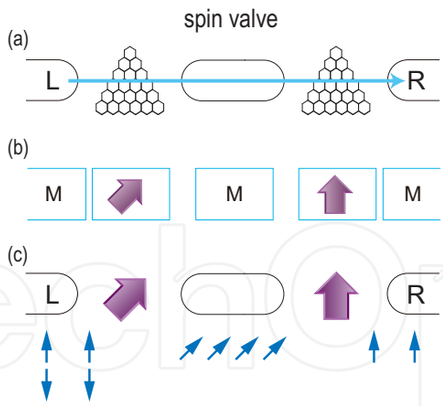

Fig. 23. Illustration of spin valve. (a) The spin valve is made of two nanodisks with the same size, which are connected with leads. (b) The system is analogous to the one made of metals and ferromagnets. (c) Applying external magnetic field, we control the spin direction of the first nanodisk to be $|\theta\rangle$, and that of the second nanodisk to be $|0\rangle = |\uparrow\rangle$. The incomming current is unpolarized, but the outgoing current is polarized, $I_{\uparrow}^{\text{out}} = I\cos\frac{\theta}{2}$, $I_{\downarrow}^{\text{out}} = 0$. Its magnitude can be controlled continuously. This acts as a spin valve.

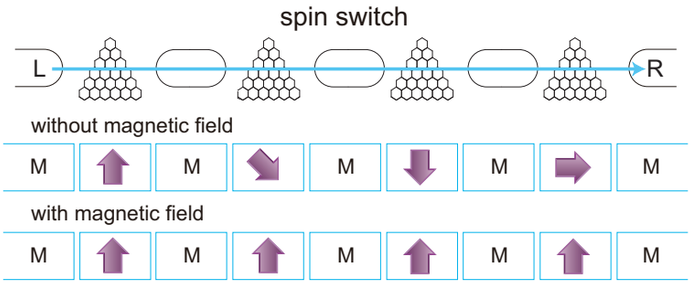

Fig. 24. A chain of nonodisks and leads acts as a spin switch. Without external magnetic field, nanodisk spins are oriented randomly due to thermal fluctuations, and a current cannot go through the chain. However, as soon as a uniform magnetic field is applied to all nanodisks, the direction of all nanodisk spins become identical and a current can go through.

current cannot go through the chain. However, when and only when a uniform magnetic field is applied to all nanodisks, the direction of all nanodisk spins become identical and a current can go through. Thus the system acts as a spin switch, showing a giant magnetoresistance effect. The advantage of this system is that a detailed control of magnetic field is not necessary in each nanodisk.

8.0.0.6 Spin-field-effect transistor

We again set up a system composed of two nanodisks sequentially connected with leads [Fig.25]. We now apply the same external magnetic field to both these nanodisks, and fix their spin direction to be up, $|0\rangle = |\uparrow\rangle$. As an additional setting, we use a lead acting as a spin rotator with the spin-rotation angle θ. The outgoing current from the second nanodisk is $I_{\uparrow}^{\text{out}} = I\cos\frac{\theta}{2}$. It is possible to tune the angle θ by applying an electric field. Hence we can control the magnitude of the up-polarized current. The system acts as a spin-field-effect transistor(79).

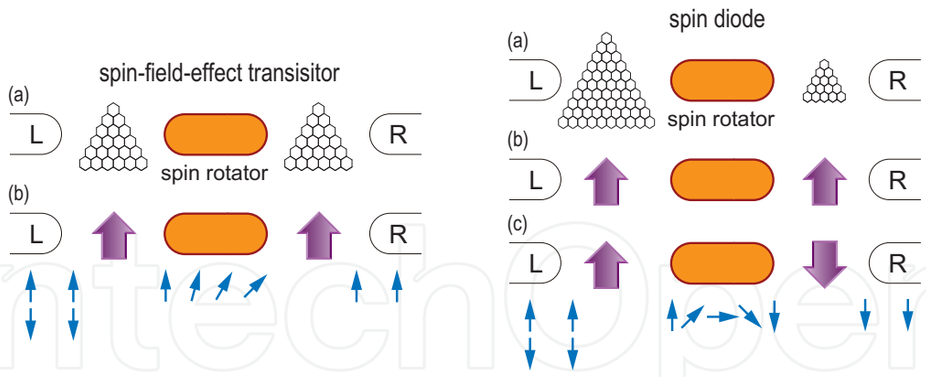

Fig. 25. (Left) Illustration of spin-field-effect transistor made of two nanodisks with the same size. Two nanodisks are connected with a rotator. We set the spin direction of the two nanodisks to be up by magnetic field. The incomming current is unpolarized, but the outgoing current is polarized and given by $I_{\uparrow}^{\rm out} = I\cos\frac{\theta}{2}$, $I_{\downarrow}^{\rm out} = 0$. The up-spin current is rotated by the angle θ within the central lead ascting as a rotator. Illustration of spin diode made of two nanodisks with different size. By controlling the bias voltage $\Delta\mu$, the current flows from the left lead to the right lead ($\Delta\mu > 0$), or in the opposite way ($\Delta\mu < 0$). The incoming current is unpolarized, which is made polarized by the first nanodisk. The electron spin in the central lead is rotated by the Rashba-type interaction. (Right) Illustration of spin diode made of two nanodisks with different size. By controlling the bias voltage $\Delta\mu$, the current flows from the left lead to the right lead ($\Delta\mu > 0$), or in the opposite way ($\Delta\mu < 0$). The incoming current is unpolarized, which is made polarized by the first nanodisk. The electron spin in the central lead is rotated by the Rashba-type interaction.

8.0.0.7 Spin diode

The third example is a spin diode [Fig.25]. We set up a system composed of two nanodisks sequentially connected with leads, where two nanodisks have different sizes. The left nanodisk is assumed to be larger than the right nanodisk. Then the relaxation time of the left nanodisk $\tau_{\rm L}(\equiv \tau_{\rm filter}^{\rm L})$ is larger than that of the right nanodisk $\tau_{\rm R}(\equiv \tau_{\rm filter}^{\rm R})$, $\tau_{\rm L} > \tau_{\rm R}$. Second, the applied magnetic field is assumed to be so small that the nanodisk spin can be controlled by a polarized current. For definiteness we take the direction of the magnetic field to be up. Third, the lead is assumed to have the Rashba-type interaction(80),

$$H_{\rm R} = \frac{\lambda}{\hbar}\left(p_x\sigma^y - p_y\sigma^x\right). \tag{75}$$

Spins make precession while they pass through the lead. The spin-rotation angle is given(55) by

$$\Delta\theta = \frac{2\lambda m^* L}{\hbar}, \tag{76}$$

where m^* is the electron effective mass in the lead and L is the length of the lead. We can control $\Delta\theta$ by changing the coupling strength λ externally by applying electric field(81).
When no currents enter the nanodisk, the direction of two nanodisk spins is identical due to the tiny external magnetic field, which is up. When we inject the current in this state, the net outgoing current is very small,

$$I^{\rm out} = \cos\Delta\theta \simeq 0 \qquad \text{for} \quad \Delta\theta \approx \pi. \tag{77}$$

This is the "off" state of the spin diode.
Let us inject an unpolarized pulse square current to the system, starting at $t = t_i$ and finishing at $t = t_f$,

$$I_\sigma(t) = I^{\text{in}}\theta(t - t_i)\theta(t_f - t), \tag{78}$$

where σ denotes the spin. The system become the "on" state by the pulse. When the bias voltage is such that $\Delta\mu > 0$, the current flows into the left nanodisk and then into the right nanodisk. The left nanodisk acts as a spin filter. The current in the central lead is initially up-polarized but is rotated by the angle $\Delta\theta$ due to the Rashba-type coupling effect. Then it enters the right nanodisk. This rotation angle acts as the initial phase for the second nanodisk. On the other hand, when $\Delta\mu < 0$, the current enters the right nanodisk and goes out from the left nanodisk. Since the relaxation time is τ_{L}, the total spin-dependent charge is given by the above formulas but with the replacement of τ_{R} by τ_{L}. Because the sizes of two nanodisks are different, these two currents behave in a different way.
The important result is that the system acts as a rectifier so that the up-spin current flows from the left to the right, or the large nanodisk to the small nanodisk. We may call it "spin diode".

9. Discussions

The physics of graphene related materials is currently one of the most active and attractive research areas in condensed matter physics. Among these graphene derivatives nanoribbons and nanodisks are mainly focused. They correspond to wires and quantum dots, respectively. There are a profusion of papers on nanoribbons, but there are yet only a few works on nanodisks. This may be because nanodisks are difficult to manufacture. However, nanodisks are experimentally isolated recently by the Ni etching techniques. An experimental realization must accelerate both experimental and theoritical studies on nanodisks.
In this paper we have reported the results on the electronic and magnetic properties of nanodisks. The trigonal zigzag nanodisk has N-fold degenerate zero-energy states when its size is N. The low-energy physics near the Fermi energy is well described by this zero-energy sector. Wave functions are explicitly constructed and classified according to the symmetry group C_{3v}. The emergence of a quasi-phase transition has been found between the quasi-ferromagnet and the paramagnet as a function of temperature even for samples with $N \approx 100$. We have also studied nanodisk-lead systems. In the intermediate coupling regime, as the chemical potential increases, a salient series of Coulomb blockade peaks develops in the conductance, reflecting the energy spectrum of nanodisk with a broken SU(N) symmetry. An appropriate size to observe Coulomb blockades is $N = 2 \sim 10$. In the strong coupling regime, by investigating the spin-spin correlation, we present some indications of many-spin Kondo effects. An appropriate size to observe Kondo effects is $N = 2 \sim 4$.

10. Acknowledgements

I am very much grateful to Professors N. Nagaosa, T. Ando, S. Tarucha, Y. Takada, H. Tsunetsugu, A. Oshiyama, M. Ueda, S. Hasegawa, P. Kim, P.J. Herrero, B. Nikolic and C. Honerkamp for fruitful discussions on the subject and reading through the manuscript. This work was supported in part by Grants-in-Aid for Scientific Research from the Ministry of Education, Science, Sports and Culture 20840011, No. 20940011 and No. 22740196.

11. References

[1] M. S. Dresselhaus, G. Dresselhaus, K. Sugihara, I. L. Spain and H. A. Goldberg, *Graphite Fibers and Filaments*, Springer Series in Material Science Vol 5 (Springer-Verlag, Berlin, 1988).

[2] J. W. McClure, Phys.Rev. 104, 666 (1956).

[3] S. Iijima, Nature (London) 354, 56 (1991).

[4] N. Hamada, S. I. Sawada, and A. Oshiyama, Phys. Rev. Lett. 68, 1579 (1992).

[5] R. Saito, M. Fujita, G. Dresselhaus, and M. S. Dresselhaus, Appl. Phys. Lett. 60, 18 (1992).

[6] J. W. Mintmire, B. I. Dunlap, and C. T. White, Phys. Rev. Lett. 68, 631 (1992).

[7] R. Saito, G. Dresselhaus, and M. S. Dresselhaus, *Physical Properties of Carbon Nanotubes*, Imperial College Press, 1998, London.

[8] J. W. G. Wildöer, L. C. Venema, A. G. Rinzler, R. E. Smalley, and C. Dekker, Nature (London) 391, 59 (1998).

[9] A. Jorio, R. Saito, J. H. Hafner, C. M. Lieber, M. Hunter, T. McClure, G. Dresselhaus, and M. S. Dresselhaus, Phys. Rev. Lett. 86, 1118 (2001).

[10] M. Ouyang, J. L. Huang, C. M. Lieber, Ann. Rev. Phys. Chem 53, 201 (2002).

[11] H. W. Kroto, J. R. Heath, S. C. O'Brien, R. F. Curl, R. E. Smalley, Nature (London) 318, 167 (1985).

[12] K.S. Novoselov, A. K. Geim, S. V. Morozov, D. Jiang, Y. Zhang, S. V. Dubonos, I. V. Grigorieva, and A. A. Firsov, Science 306, 666 (2004).

[13] K.S. Novoselov, A. K. Geim1, S. V. Morozov, D. Jiang1, M. I. Katsnelson, I. V. Grigorieva, S. V. Dubonos and A. A. Firsov, Nature 438, 197 (2005).

[14] Y. Zhang, Yan-Wen Tan, Horst L. Stormer and Philip Kim, Nature 438, 201 (2005).

[15] A. H. Castro Neto, F. Guinea, N. M. R. Peres, K. S. Novoselov and A. K. Geim, Rev. Mod. Phys. 81, 109 (2009).

[16] D. J. Klein, Chem. Phys. Lett. 217, 261 (1994).

[17] M. Fujita, K. Wakabayashi, K. Nakada, and K. Kusakabe, J. Phys. Soc. Jpn. 65, 1920 (1996).

[18] Y. Niimi, T. Matsui, H. Kambara, K. Tagami, M. Tsukada, and H. Fukuyama. Appl. Surf. Sci. 241, 43 (2005). Y. Kobayashi, K. Fukui, T. Enoki and K. Kusakabe, Phys. Rev. B, 73, 125415 (2006).

[19] O. E. Andersson, B. L. V. Prasad, H. Sato, T. Enoki, Y. Hishiyama, Y. Kaburagi, M. Yoshikawa and S. Bandow, Phys. Rev. B, 58, 16387 (1998).

[20] K. Kusakabe and M. Maruyama, Phys. Rev. B, 67, 092406 (2003).

[21] M. Ezawa, Physical Review B, 73, 045432 (2006).

[22] L. Brey, and H. A. Fertig, Phys. Rev. B, 73, 235411 (2006).

[23] F. Muñoz-Rojas, D. Jacob, J. Fernández-Rossier, and J. J. Palacios, Phys. Rev. B, 74, 195417 (2006).

[24] Y. -W Son, M. L. Cohen, and S. G. Louie, Phys. Rev. Lett., 97, 216803 (2006).

[25] V. Barone, O. Hod, and G. E. Scuseria, Nano Lett., 6, 2748 (2006).

[26] M. Y. Han, B. Oezyilmaz, Y. Zhang, and P. Kim, Phys. Rev. Lett., 98, 206805 (2007).

[27] Z. Chen, Y. -M. Lin, M. J. Rooks, and P. Avouris, Physica E, 40, 228 (2007).

[28] Z. Xu and Q. -S. Zheng, Appl. Phys. Lett. 90, 223115 (2007).

[29] B. Özyilmaz, P. Jarillo-Herrero, D. Efetov and P. Kim, Appl. Phys. Lett. 91, 192107 (2007).
[30] Y.W. Son, M.L. Cohen and S.G. LouieSon, Nature 444, 347 (2006).
[31] O.Hod, V. Barone, J.E. Peralta and G.E. Scuseria, Nano Lett. 7, 2295 (2007).
[32] See http://sciencewatch.com/ana/st/graphene/.
[33] C. Berger, Z. Song, X. Li, X. Wu, N. Brown, C. Naud, D. Mayou, T. Li, J. Hass, A.N. Marchenkov, E. H. Conrad, P.N. First and W. A. de Heer, Science 312, 119 (2006).
[34] H. J. Räder, A. Rouhanipour, A. M. Talarico, V. Palermo, P. Samorì, and K. Müllen, Nature materials 5, 276 (2006).
[35] M. Ezawa, Physica Status Solidi (c) 4, No.2, 489 (2007).
[36] M. Ezawa, Phys. Rev. B 76, 245415 (2007): M. Ezawa, Physica E 40, 1421-1423 (2008).
[37] J. Fernández-Rossier, and J. J. Palacios, Phys. Rev. Lett. 99, 177204 (2007).
[38] W. L. Wang, S. Meng, and E. Kaxiras, Nano Lett 8, 241 (2008).
[39] W. L. Wang, Oleg V. Yazyev, S. Meng, and E. Kaxiras, Phys. Rev. Lett. 102, 157201 (2009).
[40] J. Akola, H. P. Heiskanen, and M. Manninen, Phys. Rev. B 77, 193410 (2008).
[41] O. V. Yazyev, Rep. Prog. Phys 73, 5 (2010).
[42] A. D. Güçlü, P. Potasz, O. Voznyy, M. Korkusinski, and P. Hawrylak, Phys. Rev. Lett. 103, 246805 (2009).
[43] P. Potasz, A. D. Güçlü and P. Hawrylak, Phys. Rev. B 81, 033403 (2010).
[44] L. C. Campos, V. R. Manfrinato, J. D. Sanchez-Yamagishi, J. Kong and P. Jarillo-Herrero, Nano Lett., 9, 2600 (2009).
[45] O. Hod, V. Barone, and G. E. Scuseria, Phys. Rev. B 77, 035411 (2008).
[46] M. Ezawa, Phys. Rev. B 77, 155411 (2008).
[47] M. Ezawa, Phys. Rev. B 79, 241407(R) (2009).
[48] M. Ezawa, Phys. Rev. B 81, 201402(R) (2010).
[49] J.C. Slonczewski and P.R. Weiss, Phys. Rev. 109, 272 (1958).
[50] G. W. Semenoff, Phys. Rev. Lett. 53, 2449 (1984).
[51] H. Ajiki and T. Ando, J. Phys. Soc. Jpn., 62, 1255 (1993); T. Ando, Y. Zheng and H. Suzuura, Microelectronic Engineering, 63, 167 (2002).
[52] S. Murakami, N. Nagaosa, S.-C. Zhang, Science 301, 1348 (2003).
[53] Y. Ohno, D. K. Young, B. Beschoten, F. Matsukura, H. Ohno and D. D. Awschalom, Nature 402, 790 (1999).
[54] See, e.g., Realizing Controllable Quantum States: Mesoscopic Superconductivity and Spintronics, edited by H. Takayanagi and J. Nitta, World Scientific, Singapore, 2005, and references therein.
[55] I. Zŭtić, J. Fabian and S. Das Sarma, Rev. Mod. Phys., 76, (2004), and references therin.
[56] S. A. Wolf, D. D. Awschalom, R. A. Buhrman, J. M. Daughton, S. von Molnár, M.L.Roukes, A. Y. Chtchelkanova and D. M. Treger, Science 294, 1488 (2001), and references therin.
[57] G. A. Prinz, Science 282, 1660 (1998), and references therin.
[58] P. Recher, E. V. Sukhorukov and D. Loss, Phys. Rev. Lett., 85, 1962 (2000).
[59] J. A. Folk, R. M. Potok, C. M. Marcus and V. Umansky, Science 299, 679 (2003).
[60] N. Tombros, C. Jozsa, M. Popinciuc, H. T. Jonkman, B. J. van Wees, Nature 448, 571 (2007).

[61] V. M. Karpan, G. Giovannetti, P. A. Khomyakov, M. Talanana, A. A. Starikov, M. Zwierzycki, J. van den Brink, G. Brocks, P. J. Kelly, Phys Rev Lett 99, 176602 (2007).

[62] L.Brey, H.A.Fertig, Phys. Rev. B 76, 205435 (2007).

[63] M. Wimmer, N. Adagideli, S. Berber, D. Tománek, and K. Richter, Phys. Rev. Lett., 100, 177207 (2008).

[64] M. Ezawa, Eur. Phys. J. B 67, 543 (2009).

[65] M. Ezawa, New J. Phys., 11, 095005 (2009).

[66] M. Ezawa, Physica E 42, 703-706 (2010).

[67] K.S. Novoselov, E. McCann, S. V. Morozov, V. I. Fal'ko, M. I. Katsnelson, U. Zeitler, D. Jiang, F. Schendini and A. K. Geim, Nature Phys. 2, 177 (2006).

[68] S. Fajtlowicz, P. E. John, and H. Sachs, Croat. Chem. Acta 78, 195. (2005).

[69] S.Y. Zhou, G.-H. Gweon, J. Graf, A. V. Fedorov, C. D. Spataru, R. D. Diehl, Y. Kopelevich, D.-H. Lee, S.G. Louie, A. Lanzara, Nature Phys. 2, 595 (2006).

[70] T. Matsuda, S. Hasegawa, M. Igarashi, T. Kobayashi, M. Naito, H. Kajiyama, J. Endo, N. Osakabe and A. Tonomura, Phys. Rev. Lett. 62, 2519 (1989).

[71] M. Kinza, J. Ortlo, and C. Honerkamp, cond-mat/arXiv:1002.2513

[72] E. H. Lieb, Phys. Rev. Lett. 62, 1201 (1989).

[73] L. Pisani, J.A. Chan, B. Montanari and N.M. Harrison, Phys. Rev. B 75, 64418 (2007).

[74] J. P. Hobson and W. A. Nierenberg, Phys. Rev. 89, 662 (1953).

[75] T. Koga, J. Nitta, H. Takayanagi and S. Datta, Phys. Rev. Lett. 88, 126601 (2002).

[76] M. N. Baibich, J. M. Brot, A. Fert, N. V. Dau and F. Petroff, Phys. Rev. Lett. 61, 2472 (1988).

[77] G. Binasch, P. Grunberg, F. Saurenbach and W. Zinn, Phys. Rev. B 39, 4828 (1989).

[78] Y. M. Lee, J. Hayakawa, S. Ikeda, F. Matsukura and H. Ohno, Appl. Phys. Lett. 90, 212507 (2007).

[79] S. Datta and B. Das, Appl. Phys. Lett. 56, 665 (1990).

[80] E. I. Rashba, Fiz. Tverd. Tela (Leningrad) 2, 1224 (1960) [Sov. Phys. Solid State 2, 1109 (1960)]; Y. A. Bychkov and E. I. Rashba, J. Phys. C 17, 6039 (1984).

[81] J. Nitta, T. Akazaki, and H. Takayanagi, Phys. Rev. Lett. 78, 1335 (1997).

IntechOpen

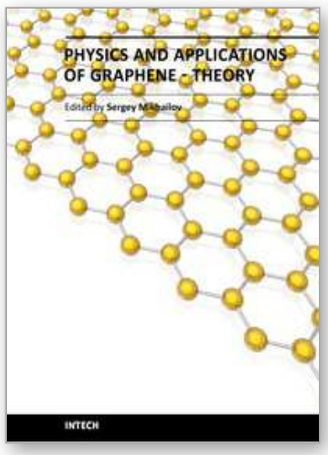

Physics and Applications of Graphene - Theory

Edited by Dr. Sergey Mikhailov

ISBN 978-953-307-152-7
Hard cover, 534 pages
Publisher InTech
Published online 22, March, 2011
Published in print edition March, 2011

The Stone Age, the Bronze Age, the Iron Age... Every global epoch in the history of the mankind is characterized by materials used in it. In 2004 a new era in material science was opened: the era of graphene or, more generally, of two-dimensional materials. Graphene is the strongest and the most stretchable known material, it has the record thermal conductivity and the very high mobility of charge carriers. It demonstrates many interesting fundamental physical effects and promises a lot of applications, among which are conductive ink, terahertz transistors, ultrafast photodetectors and bendable touch screens. In 2010 Andre Geim and Konstantin Novoselov were awarded the Nobel Prize in Physics "for groundbreaking experiments regarding the two-dimensional material graphene". The two volumes Physics and Applications of Graphene - Experiments and Physics and Applications of Graphene - Theory contain a collection of research articles reporting on different aspects of experimental and theoretical studies of this new material.

How to reference

In order to correctly reference this scholarly work, feel free to copy and paste the following:

Motohiko Ezawa (2011). Physics of Triangular Graphene, Physics and Applications of Graphene - Theory, Dr. Sergey Mikhailov (Ed.), ISBN: 978-953-307-152-7, InTech, Available from: http://www.intechopen.com/books/physics-and-applications-of-graphene-theory/physics-of-triangular-graphene

INTECH
open science | open minds

InTech Europe
University Campus STeP Ri
Slavka Krautzeka 83/A
51000 Rijeka, Croatia
Phone: +385 (51) 770 447
Fax: +385 (51) 686 166
www.intechopen.com

InTech China
Unit 405, Office Block, Hotel Equatorial Shanghai
No.65, Yan An Road (West), Shanghai, 200040, China
中国上海市延安西路65号上海国际贵都大饭店办公楼405单元
Phone: +86-21-62489820
Fax: +86-21-62489821

© 2011 The Author(s). Licensee IntechOpen. This chapter is distributed under the terms of the Creative Commons Attribution-NonCommercial-ShareAlike-3.0 License, which permits use, distribution and reproduction for non-commercial purposes, provided the original is properly cited and derivative works building on this content are distributed under the same license.

IntechOpen

IntechOpen